Original Article

CAMBRIDGE
UNIVERSITY PRESS

Triassic trachytic volcanism in the Bangong–Nujiang Ocean: geochemical and geochronological constraints on a continental rifting event

Ming Zheng[1,2] ⬤, Yang Song[1] ⬤, Haifeng Li[1,3], Carl Guilmette[4], Juxing Tang[1], Qing Zhang[5], Zhibo Liu[1] and Faqiao Li[1]

[1]Institute of Mineral Resources, Chinese Academy of Geological Sciences, Beijing 100037, China; [2]School of Resources and Environmental Engineering, Hefei University of Technology, Hefei 230009, China; [3]China 19th Metallurgical Corporation, Chengdu 610031, China; [4]E4M, Département de Géologie et Génie Géologique, Université Laval, 1065 Avenue de la Médecine, Québec, Québec G1V0A6, Canada and [5]Institute of Geology and Geophysics, Chinese Academy of Sciences, Beijing 100029, China

Abstract

The Bangong–Nujiang suture zone (BNSZ), which separates the Gondwana-derived Qiangtang and Lhasa terranes, preserves limited geological records of the Bangong–Nujiang Ocean (BNO). The timing of opening of this ocean has been hotly debated due to the rare and complicated rock records in the suture zones, which span over 100 Ma from Carboniferous–Permian to Early Jurassic time, based on geological, palaeontological and palaeomagnetic data. A combination of geochemical, geochronological and isotopic data are reported for the Riasairi trachytes, central BNSZ, northern Tibet, to constrain its petrogenesis and tectonic settings. Zircon U–Pb dating by laser ablation inductively coupled plasma mass spectrometry (LA-ICP-MS) yields mean ages of 236 Ma. Geochemically, these rocks are high-K calc-alkaline with moderate SiO_2 (59.1–67.5 wt%) and high $K_2O + Na_2O$ (8.1–11.6 wt%) contents. They are enriched in light rare earth elements with negative Eu anomalies, and show enrichments in high-field-strength elements with positive 'Nb, Ta' anomalies, similar to the intra-continental rift setting-related felsic lavas from the African Rift System. The high positive zircon $\epsilon_{Hf}(t)$ and bulk $\epsilon_{Nd}(t)$ values, as well as high initial Pb isotopes, imply a heterogeneous source involving both asthenospheric and subcontinental lithospheric mantle. The field and geochemical data jointly suggest that the Riasairi trachytes within the Mugagangri Group were formed in a continental rift setting. We interpret that the continental-rift-related Riaisairi trachytic lavas as derived from the southern margin of the Qiangtang terrane, implying that the BNO would have opened by Middle Triassic time, well after the commonly interpreted break-up of the Qiangtang terrane from Gondwana.

1. Introduction

The central Tibetan Plateau consists of the Gondwana-derived Qiangtang and Lhasa terranes that migrated N-wards and sequentially accreted during the Mesozoic Era. The N-wards transfer of these terranes was accommodated by the birth and destruction of major oceanic basins, the remnants of which are now exposed in the Indus–Yarlung Zangbo and Bangong–Nujiang Suture Zone (Dewey & Burke, 1973; Metcalfe, 2011). Reconstructing the evolution of these oceanic domains is difficult because the geological archives are poorly preserved in challenging terrain (Kapp & Decelles, 2019; Li *et al.* 2019c). The Bangong–Nujiang suture zone (BNSZ) in central Tibet is *c.* 2000 km long trending in an E–W orientation (Fig. 1a, b). This suture zone contains remnants of the Bangong–Nujiang Ocean (BNO) (Allégre *et al.* 1984; Yin & Harrison, 2000; Li *et al.* 2006; Pan *et al.* 2006; Zhu *et al.* 2011), and this palaeo-ocean closed during Late Triassic–Early Cretaceous time when the Lhasa and Qiangtang terranes collided (Li *et al.* 2016b, 2019c).

Due to the poorly preserved rock records within the BNSZ, the initiation of the BNO has not been well constrained. Previous studies employed different lithologies and mineral studies or field observations to constrain the initiation timing, such as ophiolites (Qu *et al.* 2003; Qiu *et al.* 2004; Qiangba *et al.* 2009; Fan *et al.* 2015), abyssal or bathyal sedimentary rocks (Wang *et al.* 2002a, 2019; Pan *et al.* 2006; Hou *et al.* 2018), metamorphic rocks and subducted oceanic crust (Wang *et al.* 2015; Zhang *et al.* 2016, 2017), inherited zircons in ophiolites, island-arc assemblages (Fan *et al.* 2015) and stratigraphic unconformities (Yin & Harrison, 2000; Ren & Xiao, 2004; Pan *et al.* 2006). The above indicators gave different initiation timings for the BNO spanning over 100 Ma, from Carboniferous–Permian to Early Jurassic time (Li *et al.* 2019c).
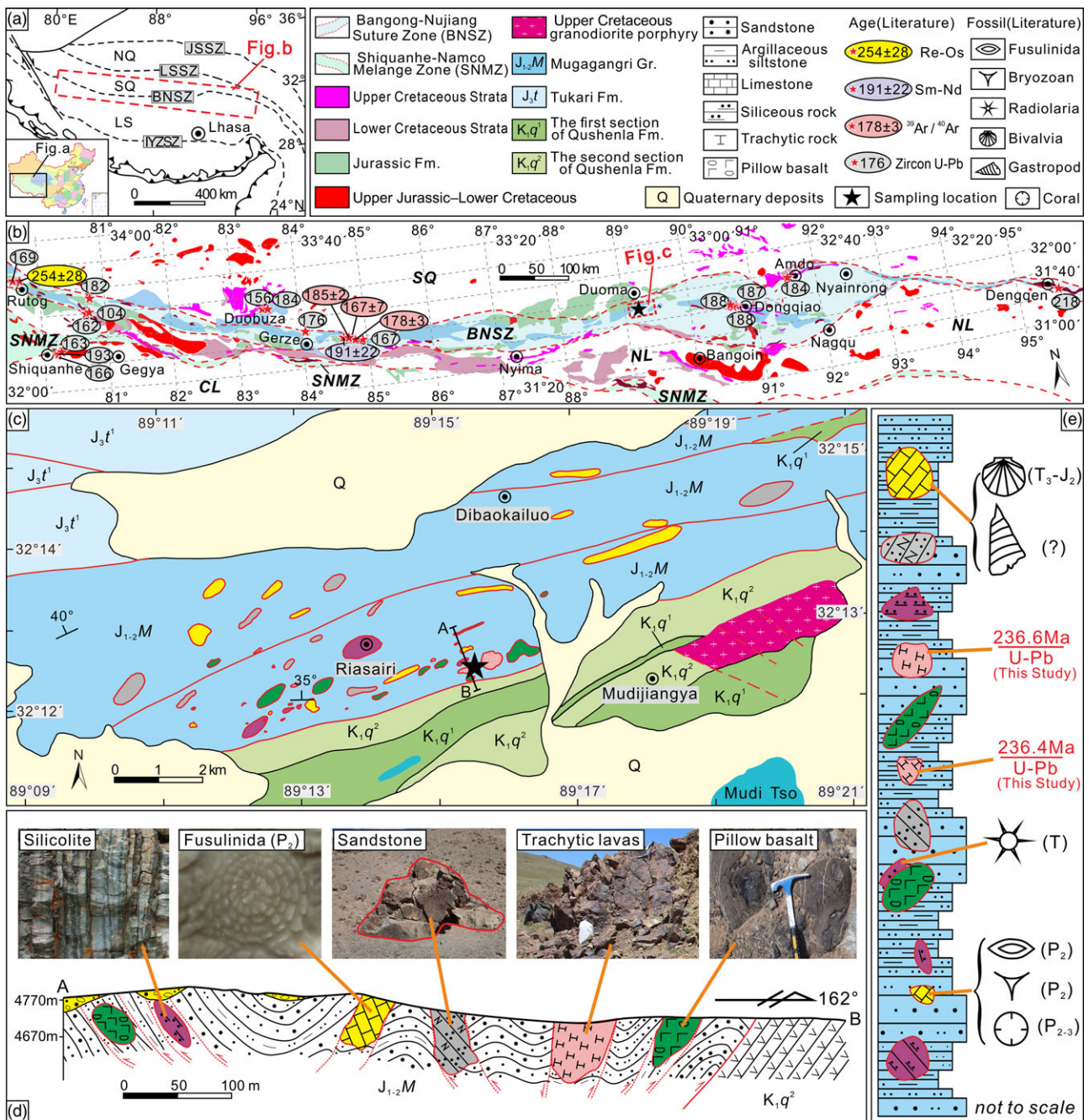
Fig. 1. (Colour online) Tectonic framework of the Tibetan Plateau and the Bangong–Nujiang suture zone (BNSZ). (a) The BNSZ in the context of the Tibetan Plateau. (b) Geological sketch map of the BNSZ. (c) Geological map of the study area. (d) Cross-section of the study area with field photographs showing prominent lithological and structural features. (e) Stratigraphic column of the Mugagangri Group in the study area. JSSZ – Jinsha suture zone; LSSZ – Longmuco–Shuanghu Lancangjiang suture zone; SNMZ – Shiquan River–Nam Tso mélange zone; IYZSZ – Indus–Yarlung Zangbo suture zone; SQ – Southern Qiangtang block; NQ – Northern Qiangtang block; LS – Lhasa terrane; NL – Northern Lhasa block; CL – Central Lhasa block; Fm – Formation; Gr – Group. Literature age data include Qiu *et al.* (2004), Huang *et al.* (2012) and Tang *et al.* (2020).

Silicic volcanism is a key component of rift magmatism and is a common product across different rift zones (Hutchison *et al.* 2018), such as the East African Rift System (EARS) (Debre Birhan: Feyissa *et al.* 2017; Rungwe: Fontijn *et al.* 2013; Axum-Adwa: Natali *et al.* 2013) and the West Antarctic Rift System (WARS) (Marie Byrd Land: Panter *et al.* 1997; LeMasurier *et al.* 2011). Such volcanism has a distinct geochemical signature reflecting fractional crystallization from a basaltic parental melt derived from partial melting of asthenospheric depleted mantle, and can therefore be dated using precise radiometric methods.

In this contribution, we focus on our newly discovered trachytic lavas in the BNSZ, which occur as clasts in a sedimentary-matrix mélange at the margin of the BNSZ, possibly recording the evolution of an intra-plate continental rift. We integrate our field observations, petrography, whole-rock geochemistry, zircon U–Pb ages, zircon Lu–Hf isotopes and whole-rock Sr–Nd–Pb isotopic data to evaluate the evolution of the now-vanished BNO to further understand the plate tectonic dance of the Lhasa and Qiangtang terranes, the two main constituents of the Tibetan Plateau.

2. First report of trachytic lava in BNSZ

The BNSZ extends over 2000 km across the central Tibetan Plateau and separates the (southern) Qiangtang terrane to the north and the Lhasa terrane to the south. We focus on the central segment of the BNSZ in Duoma town, Shuanghu County, Tibet (Fig. 1b, c). In this area, faults and structural blocks developed in the strongly deformed tectonic mélange strike NE (Fig. 1c, d). These tectonic mélanges are classified as belonging to the Jurassic Mugagangri Group, which is interpreted as an accretionary prism that formed in response to N-wards subduction of BNO oceanic lithosphere beneath the Qiangtang terrane (Zeng *et al.* 2016; Huang *et al.* 2017; Li *et al.* 2017, 2019*b*). In the study area, near Riasairi, the Mugagangri Group reaches a thickness of up to 3100 m and is a block-in-matrix mélange with strongly deformed deep-sea to bathyal turbidite deposits dominated by generally greyish-green or black-grey graywackes, lithic-quartz sandstones, mudstones and limestone, hosting apparently exotic blocks of basalt, limestone, sandstone and chert, as well as recently discovered trachytic lava blocks (Fig. 1d, e). The basalt blocks are dominated by pillow lavas occurring as a dismembered volcanic–sedimentary sequence with minor chert interlayers. Individual pillows are typically 35×55 cm in size (Fig. 1d) and blocks are generally larger than 15 m. Chert blocks are mostly medium- to thin-bedded (with bed thicknesses of 10–30 cm) and purplish-red and greyish-green in colour (Fig. 1d). The cherts contain abundant radiolarians with characteristic Triassic faunae (*Xiphosphaera sp.*, T) (Wang *et al.* 2002*b*). The limestone occurring as matrix of the sedimentary mélange contains bivalves (T_3–J_2) and gastropods (Ding, 2017). The exotic limestone blocks are mostly recrystallized micrite containing abundant fossils of Permian age, mainly fusulinidas (Fig. 1d) (*Yangchienia iniqua Lee*, P_2; *Chusenella tieni Chen*, P_2), coral (*Waagenophyllum indicum frechi Yu*, $P_{2\text{-}3}$) and bryozoans (*Fistuliramus sp.*, P_2) (Wang *et al.* 2002*b*). Sandstone blocks are in fault contact with matrix of the Mugagangri Group (Fig. 1c–e). These blocks are generally thicker than 5 m, display a massive structure of light grey colour (Fig. 2e), and are composed of quartz (58%), feldspar (24%) and lithic (volcanic) fragments (18%) (Fig. 2f).

The focal point of this study, the trachytic lava blocks occur as dismembered volcanic sequence within the mélange, with individual blocks generally thicker than 20 m. At the type locality, the main studied block is in fault contact with the clasolite matrix of the Mugagangri Group (Fig. 1c–e). Petrographically, all the volcanic samples selected from the Riasairi area are similar, in that they are predominately trachyte with minor trachyandesite (Fig. 2). The trachyandesites contain abundant plagioclase and rare pyroxene phenocrysts in a matrix of glass and fine-grained plagioclase, pyroxene and opaque minerals (mainly magnetite) (Fig. 2a, b). The trachyte lavas are characterized by the typical trachytic texture, with phenocrysts of alkali feldspar and subordinate plagioclase within a 'fluidal' groundmass consisting of unoriented microliths of alkali feldspar, subordinate opaque minerals and rare amphibole (Fig. 2c, d).

3. Analytical methods

Ten representative samples of the trachytic lavas blocks and one sandstone block sample (D2206) in Riasairi area were collected. All trachytic lavas samples were analysed for major and rare earth element (REE) abundance and Sr–Nd–Pb isotope composition. Among those, we extracted zircon from two samples of > 10 kg in order to document their U–Pb and Lu–Hf isotopic compositions. The sandstone block (sample D2206) was collected for detrital zircon U–Pb dating. The trachyte samples were trimmed to remove altered surfaces and were cleaned with deionized water before subsequent crushing into powders of *c.* 200 meshes (*c.* 75 µm) in an agate mill for analyses of major and trace elements, and Sr–Nd–Pb isotopes. Zircon grains for analysis of U–Pb and Lu–Hf isotopes were separated using conventional heavy liquid and magnetic techniques at the Langfang Regional Geological Survey, Hebei Province, China. Zircons were hand-picked under a binocular microscope and mounted in an epoxy resin disc before undergoing polishing and gold coating. Zircons were imaged under transmitted and reflected light and cathodoluminescence (CL) at the Guangzhou Institute of Geochemistry, Chinese Academy of Sciences (GIGCAS).

3.a. Whole-rock geochemical analysis

Whole-rock major and trace concentrations were analysed at ALS Minerals & ALS Chemex (Guangzhou) Co. Ltd, China. A calcined or ignited sample (*c.* 0.9 g) was added to *c.* 9.0 g lithium borate flux (50–50% $Li_2B_4O_7$–$LiBO_2$), mixed well and fused in an autofluxer at a temperature of 1050–1100 °C. A flat molten glass disk was prepared from the resulting melt. This disk is then analysed by X-ray fluorescence spectrometry (XRF) for major elements with analytical uncertainties of < 5%. For trace elements, a prepared sample (*c.* 0.2 g) is added to lithium metaborate flux (*c.* 0.9 g), mixed well and fused in a furnace at 1000 °C. The resulting melt is then cooled and dissolved in 100 mL of 4% nitric acid. This solution is then analysed by inductively coupled plasma mass spectrometry (ICP-MS) for trace elements. The analytical uncertainties were 10% for elements with abundances of < 10 ppm and approximately 5% for elements with abundances of > 10 ppm. Two standards (plagioclase amphibolite GSR-15, granitic gneiss GSR-14) were simultaneously analysed to monitor the analytical quality.

3.b. Whole-rock Sr–Nd–Pb isotopic analysis

Whole-rock Sr–Nd–Pb isotope analyses were performed at the GIGCAS. Sr and Nd isotopic compositions were determined using a micromass isoprobe multicollector (MC-) ICP-MS. Strontium and neodymium isotopic fractionation was corrected using values of $^{86}Sr/^{88}Sr = 0.1194$ and $^{146}Nd/^{144}Nd = 0.7219$, respectively. Lead isotopic compositions were measured by thermal ionization mass spectrometry (TIMS). Lead isotopic ratios were corrected for fractionation using replicate analyses of the standard NBS 981. The analytical uncertainties during the period of analysis were 0.006 for $^{206}Pb/^{204}Pb$ and $^{207}Pb/^{204}Pb$, and 0.012 for $^{208}Pb/^{204}Pb$.

3.c. Zircon U–Pb dating

The zircons were analysed for U, Th and Pb using laser ablation (LA-) ICP-MS at the Institute of Geology, Chinese Academy of Geological Sciences (IGCAGS). Before LA-ICP-MS analysis, zircon grains with fracture and inclusions were noted and avoided based on observations made using transmitted and reflected light microscopy. Prior to analysis, the surfaces of the grain mounts were then acid-washed in dilute HNO_3 and pure alcohol to remove any lead contamination. The spot size was *c.* 25 µm, and the data were calibrated according to the M127 reference zircon (U: 923 ppm; Th: 439 ppm; Th/U: 0.475). Plesovice zircon, with an age of 337.13 ± 0.37 Ma (2σ), and GJ-1 zircon with an age of 599.8 ± 1.7 Ma (2σ), were used as external standards during
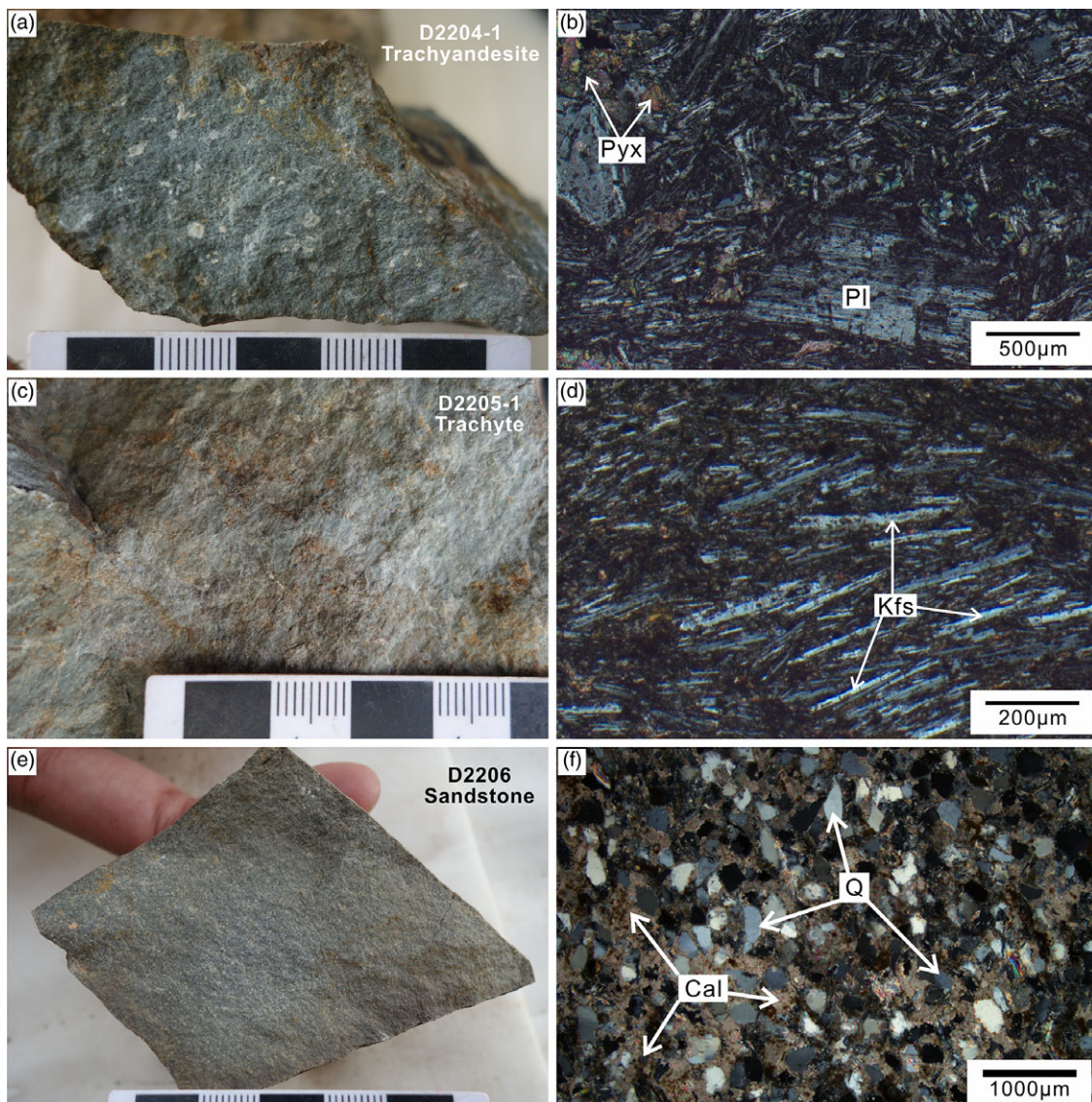
Fig. 2. (Colour online) Hand specimens photographs (left) and corresponding thin-section photomicrographs (right) of the Riasairi volcanic rocks. (a, b) Trachyandesite (D2204-1) from the Riasairi lavas. (c, d) Trachyte (D2205-1) from the Riasairi lavas. (e, f) Sandstone block (D2206) within the Mugagangri Group. Pl – plagioclase; Kfs – K-feldspar; Pyx – pyroxene; Q – quartz; Cal – calcite.

U–Pb dating and were analysed at the beginning of the run, then twice each after every five unknowns. The offline raw data selection, integration of background and analyte signals, and time-drift correction and quantitative calibration for U–Pb dating were performed by the ICPMSDataCal program. In all of the analysed zircon grains, a common Pb correction was not necessary due to the low ^{204}Pb signal and high ^{206}Pb/^{204}Pb signal.

3.d. Zircon Lu–Hf isotopic analysis

Before Lu–Hf isotopic analysis, pure alcohol was used to remove any lead contamination. Zircon Hf isotope analysis was conducted using a GeoLasPro 193 nm laser ablation microprobe that was attached to a Neptune MS-ICP-MS at IGCAGS. Lu–Hf isotopic analyses were conducted on the same zircon grains that were initially analysed, with the spot size of 44 μm. High-purity helium was used as a carrier gas to transport the ablated sample from the laser ablation cell to the ICP-MS torch via a mixing chamber that contained argon. Zircon GJ-1 was used as the reference standard

during routine analyses. GJ-1 was analysed at the beginning of the run, then twice after every five to six unknowns, yielding a weighted mean ^{176}Hf/^{177}Hf ratio of 0.282007 ± 0.000006 (2σ; $n = 14$). The calculation of Hf model ages (single-stage model ages) (T_{DM}) was based on a depleted mantle source with a present-day ^{176}Hf/^{177}Hf ratio of 0.28325 and a ^{176}Lu decay constant of 1.865×10^{-11} a^{-1}. The calculation of crustal (two-stage) Hf model ages (T_{DMC}) was based on the assumed mean ^{176}Lu/^{177}Hf value of 0.015 for the average continental crust.

4. Results

4.a. Major-element data

The results of the whole-rock chemical analyses of the Riasairi volcanic rocks are presented in online Supplementary Table S1 (available at http://journals.cambridge.org/geo). Most of the Riasairi lava samples have loss on ignition (LOI) values of < 2 wt%, indicating that they did not undergo significant alteration, as supported by the
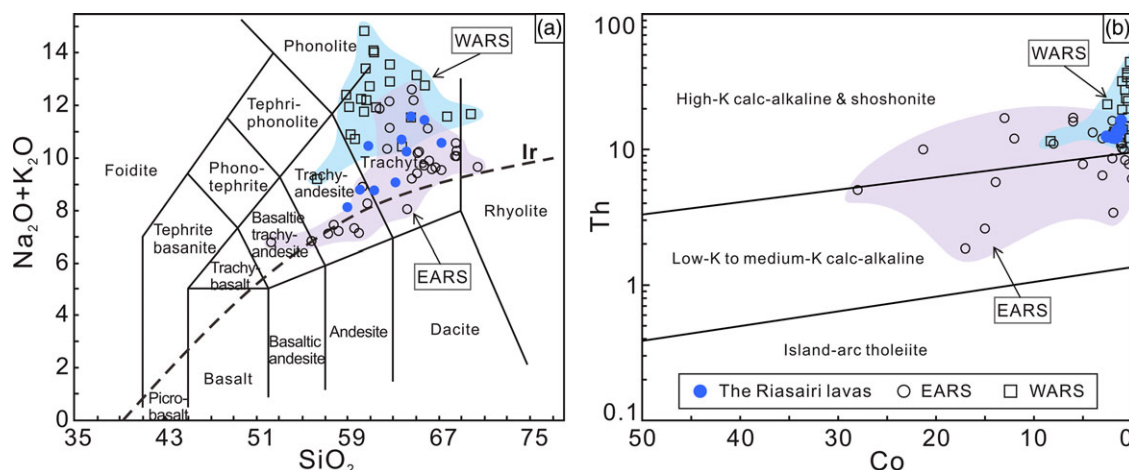
Fig. 3. (Colour online) Classification of the Riasairi volcanic rocks. (a) Total alkali silica diagram after Le Bas *et al.* (1986). (b) Co versus Th diagram after Hastie *et al.* (2007). The EARS samples are from Peccerillo *et al.* (2003), Natali *et al.* (2013), Giordano *et al.* (2014), Hutchison *et al.* (2016), Feyissa *et al.* (2017) and Corti *et al.* (2018). The WARS samples are from LeMasurier *et al.* (2011) (see online Supplementary Tables S1 and S2, available at http://journals.cambridge.org/geo, for sample details). The Ir line in (a) is based on Irvine & Baragar (1971).
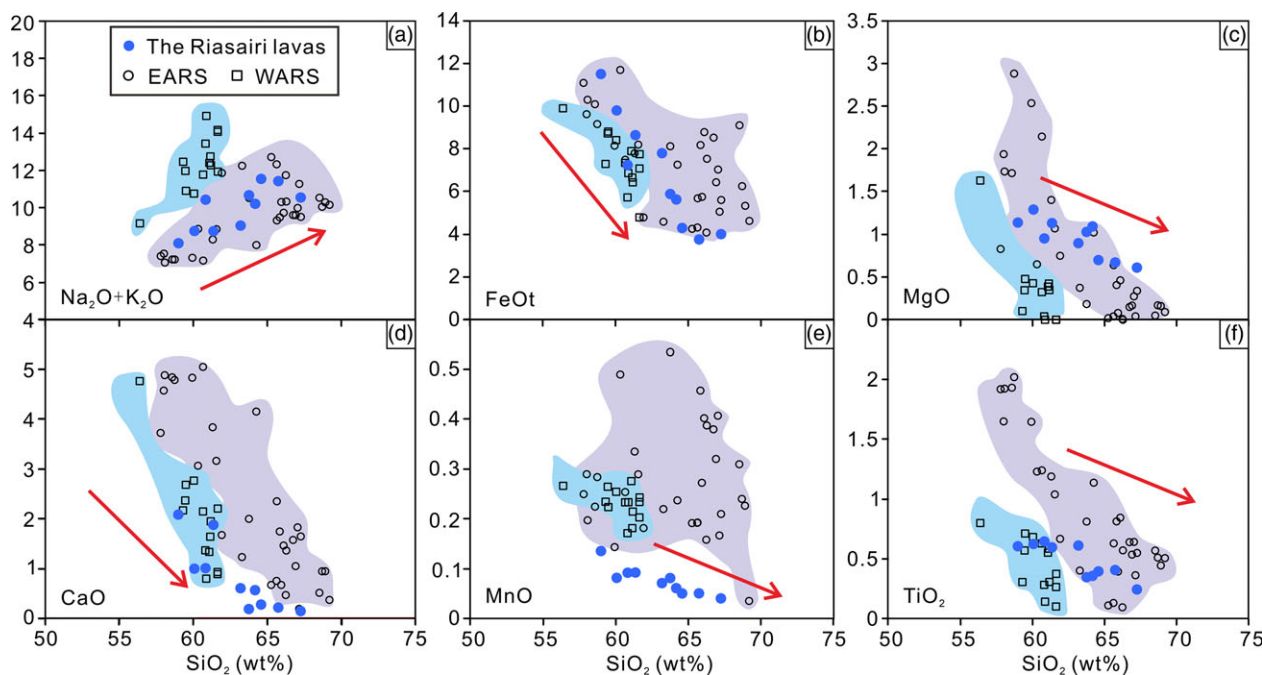

Fig. 4. (Colour online) Plots of major elements versus SiO_2 for the Riasairi volcanic rocks (see online Supplementary Tables S1 and S2). Legend as for Figure 3.

observation of unaltered matrix and phenocrysts from thin-section photomicrographs (Fig. 2a–d). On the total alkali silica diagram (TAS), all compositions cluster above the alkaline–subalkaline boundary. Most of the selected samples are trachytes, except for two samples (D2204-1, D2204-3) that plot in the trachyandesite field (Fig. 3a).

The SiO_2 contents of the samples are variable, ranging from 59 to 67 wt%. There is a positive correlation between the total alkali ($Na_2O + K_2O$) contents and SiO_2 concentrations. Major element oxides, including FeO_t, MgO, CaO, MnO and TiO_2, exhibit well-defined negative trends when plotted against SiO_2. These geochemical trends compare with those of the trachytic rocks from the EARS and WARS (Fig. 4; major- and trace-element data of EARS and WARS are summarized in online Supplementary Table S2, available at http://journals.cambridge.org/geo).

4.b. Trace elements

The Riasairi lava samples have high concentrations of incompatible elements and are enriched in light rare earth elements (LREE) ($La_N/Yb_N = 15.9–25.9$), which is a typical feature of intra-plate alkaline magmas (Panter *et al.* 1997; Chauvet *et al.* 2011). The Riasairi volcanic rocks display narrow REE patterns (Fig. 5a, c) compared with each other and are also similar to the patterns observed in some intra-continental rift setting-related felsic lavas from the EARS (Debre Birhan: Feyissa *et al.* 2017; Rungwe: Fontijn *et al.* 2013; Axum-Adwa: Natali *et al.* 2013) and the WARS (Marie Byrd Land: Panter *et al.* 1997; LeMasurier *et al.* 2011).

Primitive mantle-normalized incompatible trace-element patterns are shown in Figure 5b and d. Hutchison *et al.* (2018) documented that silicic melts generated in continental rifts by
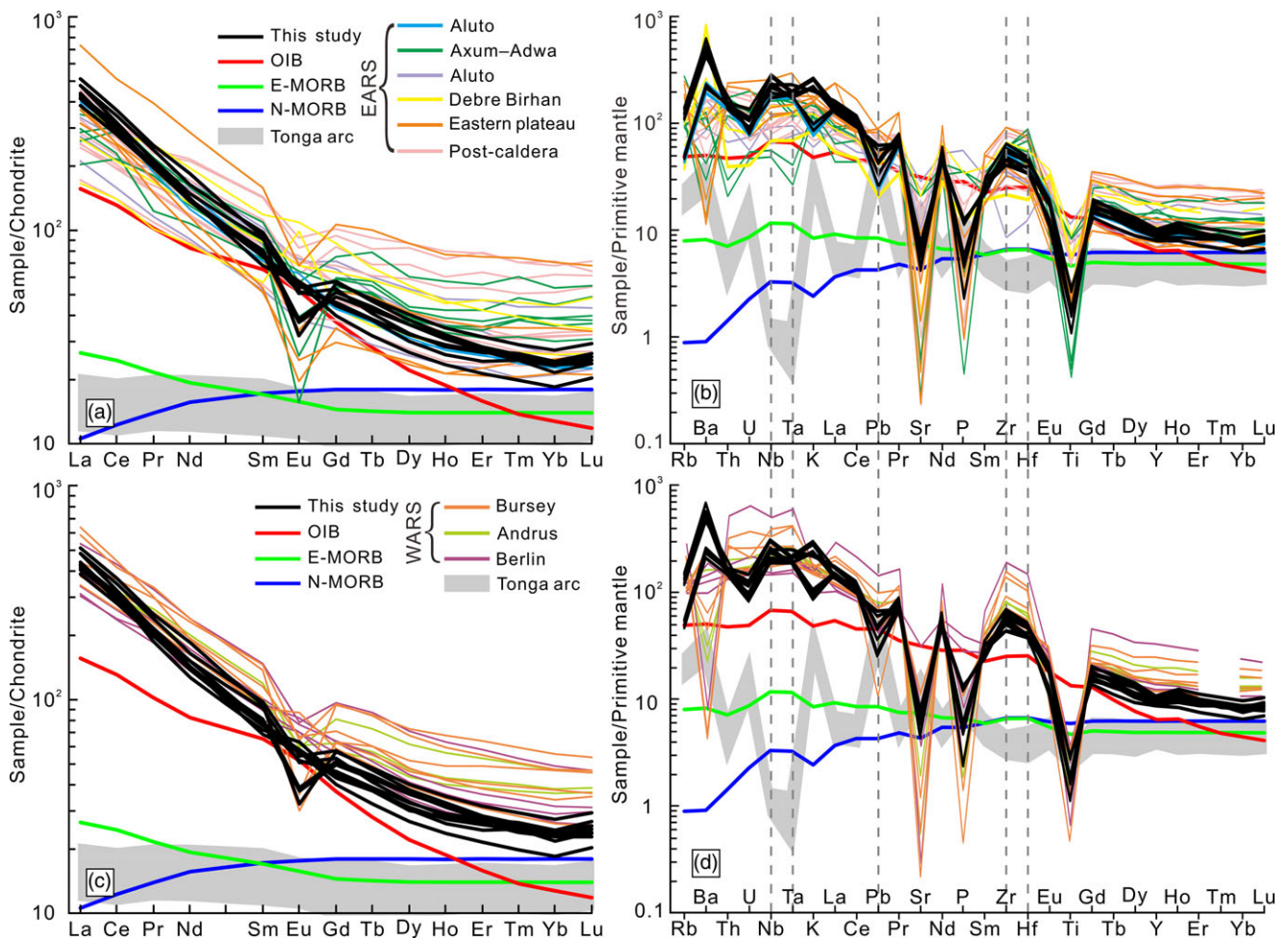
Fig. 5. (Colour online) (a, c) Chondrite-normalized REE patterns and (b, d) primitive mantle-normalized trace diagrams for the Riasairi volcanic rocks. Data sources of the EARS and WARS are as for Figure 3. Normalization values and ocean-island, enriched mid-ocean-ridge and normal mid-ocean ridge basalts (OIB, E-MORB and N-MORB) data are from Sun & McDonough (1989); Tonga arc data are from Turner et al. (2012).

protracted fractional crystallization tend to be enriched in REE, Zr, Hf, Nb and Ta, which is consistent with the Nb–Ta and Zr–Hf positive anomalies and high REE contents (up to 551 ppm, with an average of 469 ppm) observed in the Riasairi lava samples. The REE in the trachytic rocks from the study area are enriched to variable degrees: the light and heavy REE are enriched (LREE/HREE, i.e. La/Yb) by a factor of > 15, but the middle REE (i.e. Sm, Eu) are less enriched, as would be expected from apatite fractionation combined with the incorporation of Eu into feldspar (Cousens et al. 2003).

4.c. Zircon U–Pb geochronology

One trachyandesite (D2204-1) sample and one trachyte (D2205-1) sample were selected for zircon LA-ICP-MS U–Pb dating and Lu–Hf isotopic analysis. These data are listed in online Supplementary Table S3 (available at http://journals.cambridge.org/geo). The U–Pb concordia plots expressed with 1σ errors, CL and transmitted light images of representative zircon grains are shown in Figure 6a and b. The zircon grains from these two samples are colourless and transparent. Most zircons occur as euhedral stubby prismatic crystals with lengths ranging over 150–200 μm and length:width ratios of approximately 2.0. These zircon grains exhibit modest oscillatory or planar zoning in CL images, which

is a typical feature of magmatic zircons (Fig. 6a, b). The Th/U ratios of the zircons from samples 2204-1 (trachyandesite) and 2205-1 (trachyte) range from 0.85 to 1.9 and 0.64 to 1.67, respectively, also consistent with a magmatic origin (Hoskin & Black, 2000). The data obtained from 25 analyses of D2204-1 performed by LA-ICP-MS form a tight cluster on the concordia diagram with $^{206}Pb/^{238}U$ age ranging over 230.0–242.4 Ma, and yield a weighted mean age of 236.6 ± 1.7 Ma (Fig. 6a; 1σ; MSWD: 0.76), which is interpreted as the crystallization age for this sample. A total of 25 grains from sample D2205-1 were also analysed by LA-ICP-MS; all of the data points cluster together, yielding concordant $^{206}Pb/^{238}U$ ages of 228–248 Ma with a weighted mean of 236.4 ± 2.5 Ma (Fig. 6b; 1σ; MSWD = 2.5).

One sandstone sample (D2206, Fig. 2e) was collected for detrital zircon U–Pb dating (online Supplementary Table S4, available at http://journals.cambridge.org/geo). In the weighted mean age calculation using Isoplot (Ludwig, 2003), 3 of a total of 100 analyses (D2206-18, D2206-30, D2206-31) were excluded due to the low U–Pb age concordance degree; the other 97 analyses display three main age clusters at 200–1000, 1400–2100 and 2400–2750 Ma (Fig. 6c). The youngest age cluster in this sample is 218–242 Ma ($n = 5$), indicating that the maximum depositional age is Late Triassic. These five zircons exhibit an idiomorphic morphology, suggesting that they have not been transported over long distances.
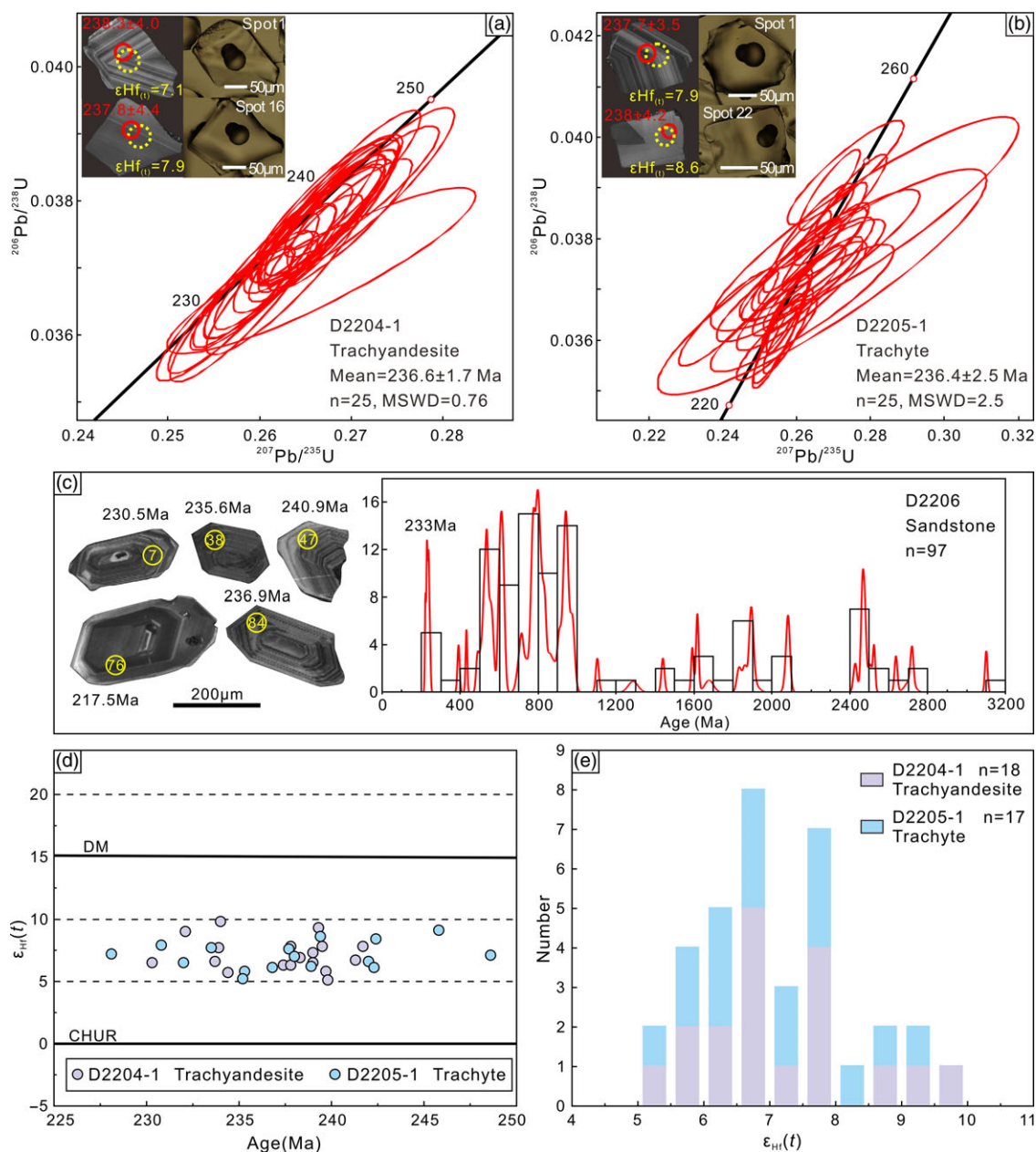
Fig. 6. (Colour online) (a, b) Representative CL and transmitted light images of dated zircons and zircon U–Pb concordia diagrams of the Riasairi volcanic rocks. (c) Representative CL images and detrital zircon age spectra for sandstone block within the Mugagangri Group. (d, e) $\epsilon_{Hf}(t)$ values for the Riasairi lavas.

These zircons exhibit typical features of magmatic zircon, with oscillatory zoning demonstrated in CL images and Th/U ratios of greater than 0.4 (Fig. 6c, Hoskin & Black, 2000).

4.d. Zircon Lu–Hf isotopic compositions

The zircon grains from the two samples (D2204-1 and D2205-1) that underwent U–Pb dating were also used for Lu–Hf isotopic analyses. The analytical results and calculations are shown in Figure 5d, e and in online Supplementary Table S5 (available at http://journals.cambridge.org/geo).

Of the 25 dated zircons from sample D2204-1 (trachyandesite), 18 were analysed for their Hf isotope ratios. This analysis yields $^{176}Hf/^{177}Hf$ and $^{176}Lu/^{177}Hf$ ratios ranging over 0.0106–0.0420 and 0.0004–0.0015, respectively, with initial $^{176}Hf/^{177}Hf$ ratios

ranging over 0.281231–0.281379 and $\epsilon_{Hf}(t)$ values varying from +5.1 to +9.8. Such isotopic compositions straddle the mean value of the depleted mantle at 607 Ma (Vervoort & Kemp, 2016). A total of 17 dated spots of the zircon grains from D2205-1 (trachyte) yield $^{176}Lu/^{177}Hf$ and $^{176}Yb/^{177}Hf$ ratios ranging over 0.0106–0.0420 and 0.0004–0.0015, respectively, with initial $^{176}Hf/^{177}Hf$ ratios ranging over 0.281231–0.281379 and $\epsilon_{Hf}(t)$ values from +5.2 to +9.1. Single-stage depleted-mantle Hf model ages (T_{DM}) are 553–695 Ma (online Supplementary Table S5, available at http://journals.cambridge.org/geo).

A total of 35 analytical locations in the two selected samples have similar Hf isotopic compositions, along with similar geochronologic and geochemical data, which demonstrate that they are derived from the same material source. Furthermore, their $\epsilon_{Hf}(t)$ values exhibit a narrow range of variation and are mainly

concentrated between +6 and +8, with all values plotting between +5 and +10 (Fig. 6d, e).

4.e. Sr, Nd and Pb isotopic compositions

A total of 10 whole-rock samples were analysed for their Sr, Nd and Pb isotopic compositions (online Supplementary Table S1, available at http://journals.cambridge.org/geo; Fig. 7). The initial Sr, Nd and Pb isotopic ratios were revised using the U–Pb zircon ages of corresponding samples. The initial $^{87}Sr/^{86}Sr$ ratios exhibit a wide range over 0.70608–0.70897 (Fig. 7a). Their Nd isotopic compositions are relatively homogeneous, with $\epsilon_{Nd}(t)$ values ranging from 3.73 to 4.10 (Fig. 7a). All of the Riasairi lava samples analysed in this study display narrow ranges of $(^{206}Pb/^{204}Pb)_i$ (18.326–18.709), $(^{207}Pb/^{204}Pb)_i$ (15.548–15.599) and $(^{208}Pb/^{204}Pb)_i$ (38.488–39.024) values. The data obtained from the investigated lavas stretch along the mantle array between the depleted mantle and the enriched lithospheric mantle (EM II, Zindler & Hart, 1986), and they plot distinctly above the Northern Hemisphere Reference Line (NHRL) of Hart (1984) in the Pb–Pb isotope diagrams (Fig. 7b, c).

5. Discussion

5.a. Crustal contamination

Ayalew *et al.* (2016) suggested that enrichment of lavas in highly and moderately incompatible elements may either be a consequence of crustal contamination of mantle-derived magma or reflect mantle sources. Negative Nb and Ta anomalies observed in primitive-mantle-normalized multi-element variation diagrams are generally interpreted as subtle tracers of crustal contamination (McClellan & Gazel, 2014; Ayalew *et al.* 2016; Corti *et al.* 2018). There are no obvious negative Nb and Ta anomalies in the Riasairi lava samples, compared with the typical intra-oceanic island arc (e.g. Tonga arc; Fig. 5b, d). The decoupling between Th and Ta is also a sensitive indicator of crustal contamination, as this process results in a marked increase in Th/Ta ratios (Condie, 1993). All of the Riasairi lavas have relatively low Th/Ta ratios (1.65–1.72), similar to those observed in intra-continental rift setting-related felsic lavas, for example, Marie Byrd Land lavas (WARS, 1.25–2.12, LeMasurier *et al.* 2011), Axum-Adwa lavas (Ethiopian plateau, 1.47–2.48, Natali *et al.* 2013), Debre Birhan lavas (Main Ethiopian Rift System, 1.15–1.50, Feyissa *et al.* 2017), Rungwe lavas (Ethiopian Rift System, 1.47–3.10, Fontijn *et al.* 2013), and Gedemsa and Fanta'Ale lavas (Ethiopian Rift System, 0.74–3.90, Peccerillo *et al.* 2003; Giordano *et al.* 2014). This provides good evidence for the Riasariri lavas being mantle derived (Th/Ta = 2.3; Condie, 1993), rather than from an upper crustal source (Th/Ta > 10). Further, it has been shown that Zr/Nb ratios remain nearly constant during fractional crystallization but change significantly during magma mixing or crustal contamination (Weaver, 1991). The Riasairi lavas show a narrow range of Zr/Nb ratios (2.9–4.9), suggesting negligible to no crustal contamination. The lavas are characterized by high contents of Nb (129–212 ppm) and Ta (7.5–10 ppm), and show Pb depletion in their primitive-mantle-normalized trace-element patterns (Fig. 5b, d), whereas continental crust is characteristically depleted in both Nb and Ta and significantly enriched in Pb. Moreover, both the upper and lower crust are known to have low Ce/Pb ratios of < 5 (Taylor & McLennan, 1985), whereas the Ce/Pb value of ocean-island and mid-ocean-ridge basalts (OIB-MORB) is *c.* 25 and that of the primitive mantle is *c.* 9 (Hofmann *et al.* 1986; Sun & McDonough, 1989; Feyissa 2017). Most of Ce/Pb values of
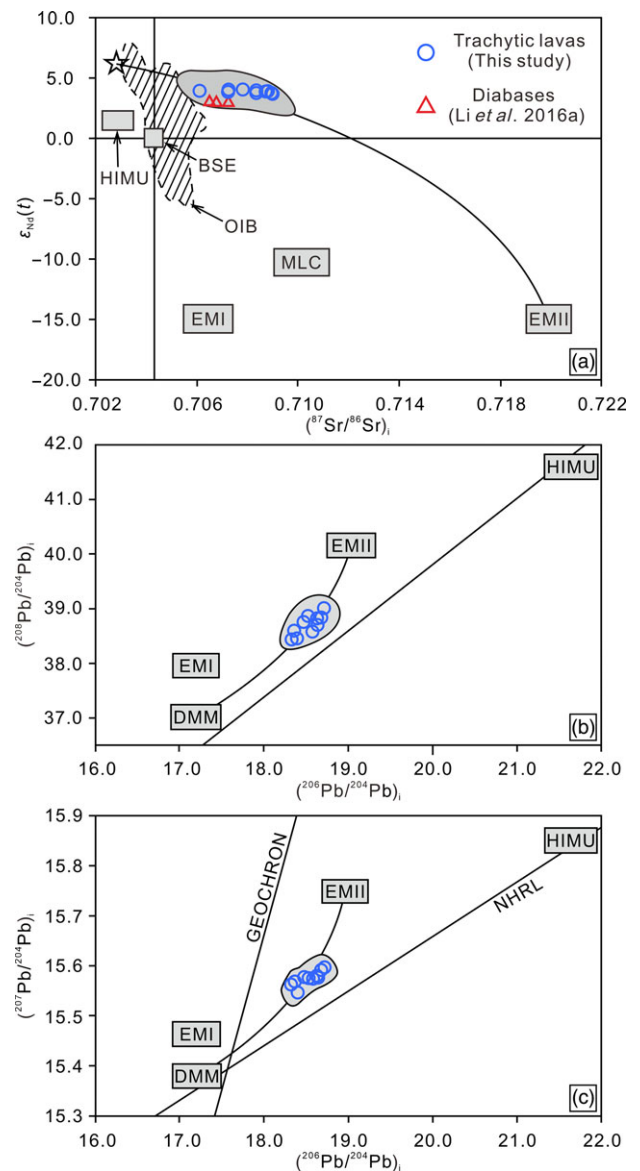

Fig. 7. (Colour online) Whole-rock Sr–Nd–Pb geochemical plots for the Riasairi volcanic rocks. (a) $(^{87}Sr/^{86}Sr)_i$ versus $\epsilon_{Nd}(t)$, (b) $(^{206}Pb/^{204}Pb)_i$ versus $(^{207}Pb/^{204}Pb)_i$, and (c) $(^{206}Pb/^{204}Pb)_i$ versus $(^{208}Pb/^{204}Pb)_i$. A typical uncontaminated asthenospheric mantle composition is marked with a star in the top left corner for (a). The fields of OIB and EMI, EMII, high-µ (HIMU) mantle components are from Zindler & Hart (1986). MLC – mean lower crust; BSE – bulk silicate earth; NHRL – Northern Hemisphere reference line, as defined by Hart (1984). The diabase data are from Li *et al.* (2016a).

the Riasairi lavas (14.2–29.6) fall within the typical mantle range and are far higher than the Ce/Pb values of the continental crust (< 5). Finally, the Riasairi samples show medium and homogeneously positive $\epsilon_{Hf}(t)$ (+5.1 to +9.8) and $\epsilon_{Nd}(t)$ (+3.73 to +4.10) values, indicating a predominantly mantle-derived melt, rather than a crust-contaminated melt. Based on these lines of evidence, we conclude that the Riasairi lavas did not undergo significant crustal contamination.

5.b. Magma source

The Riasairi lava samples show positive Nb–Ta anomalies in Figure 5, different to felsic lava from intra-oceanic island arc

(e.g. Tonga arc: Turner *et al.* 2012) but similar to the EARS (McClellan & Gazel, 2014; LeMasurier *et al.* 2011; Feyissa *et al.* 2017; Corti *et al.* 2018; Hutchison *et al.* 2018) and the WARS (Panter *et al.* 1997; LeMasurier *et al.* 2011). This suggests that the Riasairi lavas were derived from depleted asthenospheric mantle, unaffected by subduction imprint and crustal contamination (McClellan & Gazel, 2014; Corti *et al.* 2018). Without the significant role of crustal contamination as shown above, the isotope compositions of the Riasairi lava samples represent the isotopic composition of the magma source. The zircons from the Riasairi lava samples have a narrow range in their $\epsilon_{Hf}(t)$ values (+5.2 to +9.1, mainly concentrated between +6 and +8; Fig. 6d, e); these data, combined with their whole-rock geochemical data, suggest that they were mainly derived from the depleted asthenospheric mantle. In addition, these zircons have lower $\epsilon_{Hf}(t)$ values than that of the depleted mantle ($> +12$), possibly suggesting a subordinate contribution from an enriched mantle source (e.g. enriched mantle I or II (EMI or EMII)) rather than a crustal source. Sr–Nd–Pb isotopic ratios can also effectively discriminate magma sources because these are not typically modified during fractional crystallization (Shu *et al.* 2015; Ayalew *et al.* 2016). The medium and homogeneously positive $\epsilon_{Nd}(t)$ values from whole-rock samples are similar to their $\epsilon_{Hf}(t)$ values for analysed zircon grains, further supporting the theory that mixing occurred between the depleted asthenospheric mantle component and an enriched mantle component (Fig. 7a). However, modelling of asthenospheric mantle mixing with EMI does not provide an explanation for their high Sr isotopic ratios (0.706–0.709), considering that normal Sr ratios are generally less than 0.706 (Zindler & Hart, 1986; Sun & McDonough, 1989; Weaver, 1991). The proposed model of asthenospheric mantle mixing with EMII therefore provides a reasonable explanation for the origin of the Riasairi magmas within the BNSZ. This model implies the existence of EMII lithospheric mantle in the investigated area, which is support by the occurrence of the Duobuza Late Jurassic basaltic lavas that are also derived from an asthenospheric mantle source with an enriched continental lithospheric mantle (Li *et al.* 2016a). The Pb isotopic ratios of these samples stretch along the mantle array between the depleted mantle and EMII component (Fig. 7b, c), consistent with our conclusion. This explanation of the magma source being derived from asthenospheric mantle with an enriched continental lithospheric mantle component is supported by the medium and homogeneously positive $\epsilon_{Hf}(t)$ and $\epsilon_{Nd}(t)$ values, high Sr isotopic ratios and moderate Pb isotopic ratios of the samples studied here.

5.c. Petrogenesis

For the genesis of felsic magma in volcanic rift systems, two general models have been proposed: (1) the fractional crystallization of a basaltic parental magma with or without crustal assimilation; and (2) the partial melting of mafic lower crustal rocks with or without subsequent fractional crystallization (Trua *et al.* 1999; Ayalew *et al.* 2002; Feyissa *et al.* 2017). The Riasairi lavas from central BNSZ following the horizontal fractional trend as shown in a La versus La/Sm diagram (Fig. 8a). In addition, in the Ta/Yb versus Th/Yb diagram (Fig. 8b) the composition of our rocks is undistinguishable from rift volcanic rocks from both the EARS and WARS, and plot in the mantle array field. Based on these, we suggest that the composition of the Riasairi volcanic rocks is best explained by the fractional crystallization of an originally basaltic magma.

The major- and trace-element and REE characteristics of our samples are similar to those of the EARS and WARS. In terms of major elements, their lithologies are all intermediate to felsic and high-K calc-alkaline rocks, and major element oxides, including FeO_t, MgO, CaO, MnO and TiO_2, exhibit well-defined negative trends when plotted against SiO_2, and show positive correlation between the total alkali (K_2O+Na_2O) contents and SiO_2 concentrations. In terms of trace elements, the Riasairi volcanic rocks display narrow REE patterns compared with each other and are also similar to those of the EARS and WARS. These similarities further support their evolution from an originally basaltic magma by fractional crystallization without significant assimilation of crustal material (LeMasurier *et al.* 2011; Hutchison *et al.* 2018).

Fractional crystallization of basaltic melts to form trachytes is postulated to occur in intra-continental rift settings (i.e. Cousens *et al.* 2003; Ayalew *et al.* 2016): during an initial rift period, primary magma is formed by the mixing between asthenospheric and EMII lithospheric mantle sources. If eruption is prevented (e.g. insufficient thinning of the lithosphere or inadequate formation of magma pathways), such magmas may pond and rapidly fractionate in composition towards trachyte (Cousens *et al.* 2003). In both the EARS and WARS, trachytes were derived from basaltic magma rather than the mantle-derived magma (LeMasurier *et al.* 2011; Ayalew *et al.* 2016), which means that there must have been a lower magma chamber above the lithospheric mantle (Cousens *et al.* 2003; LeMasurier *et al.* 2011). In this chamber, the mantle-derived magma evolved into basaltic magma after precipitating pyroxene and olivine (Natali *et al.* 2011; Ayalew *et al.* 2016; Corti *et al.* 2018). Such an evolution is consistent with the low contents of MgO (0.6–1.26 wt%) and compatible trace elements (Ni = 0.9–6.6 ppm, V < 1–7 ppm, Sc = 3–5.4 ppm) of the Riasairi lava, indicating that these magmas underwent significant fractional crystallization within the lower magma chamber by producing olivine (Ni), Fe–Ti oxides (V) and clinopyroxene (Sc) (Cousens *et al.* 2003). In addition, the Sr, P and Ti negative anomalies in the investigated lavas (Fig. 5b, d) may be due not to their source characteristics but rather the removal of fractionating phases during the evolution of the magma, namely, plagioclase, apatite and oxides (Cousens *et al.* 2003; Natali *et al.* 2011). These effective differentiation processes imply the existence of shallow magma chambers, which is consistent with the observed phenocryst assemblages (Fig. 2) and supported by the petrogenetic model proposed by Beccaluva *et al.* (2009) and Natali *et al.* (2013), indicating that they were most likely related to the rifting tectonics and block tilting that favoured the trapping of parental magmas, leading to their fractionation towards felsic compositions. The geochemical characteristics of the felsic magma that formed by crystallization differentiation in shallow magma chambers are most closely represented by the rocks with the lowest silica contents. The rocks with low silica contents still have obvious negative Sr anomalies (Fig. 5b, d), potentially indicating the crystallization differentiation of plagioclase in shallow magma chambers, which generally produces notable negative Eu anomalies. We also noticed that four samples (D2204-1, D2204-3, D2204-4, D2205-2) show slightly positive Eu anomalies (Figs 5a, c, 8d). However, as shown in Figure 8c, the crystallization of hornblende will produce a positive anomaly, and the crystallization of a large amount of hornblende will neutralize the negative anomaly caused by the crystallization of plagioclase. The decrease in Eu/Eu* ratios with increasing silica content (Fig. 8d) suggests the occurrence of plagioclase removal during magma crystallization processes (Corti *et al.* 2018), which is consistent with the petrographic observations of large amounts of plagioclase in trachyandesites and alkali feldspar in trachytes (Fig. 2a–d).
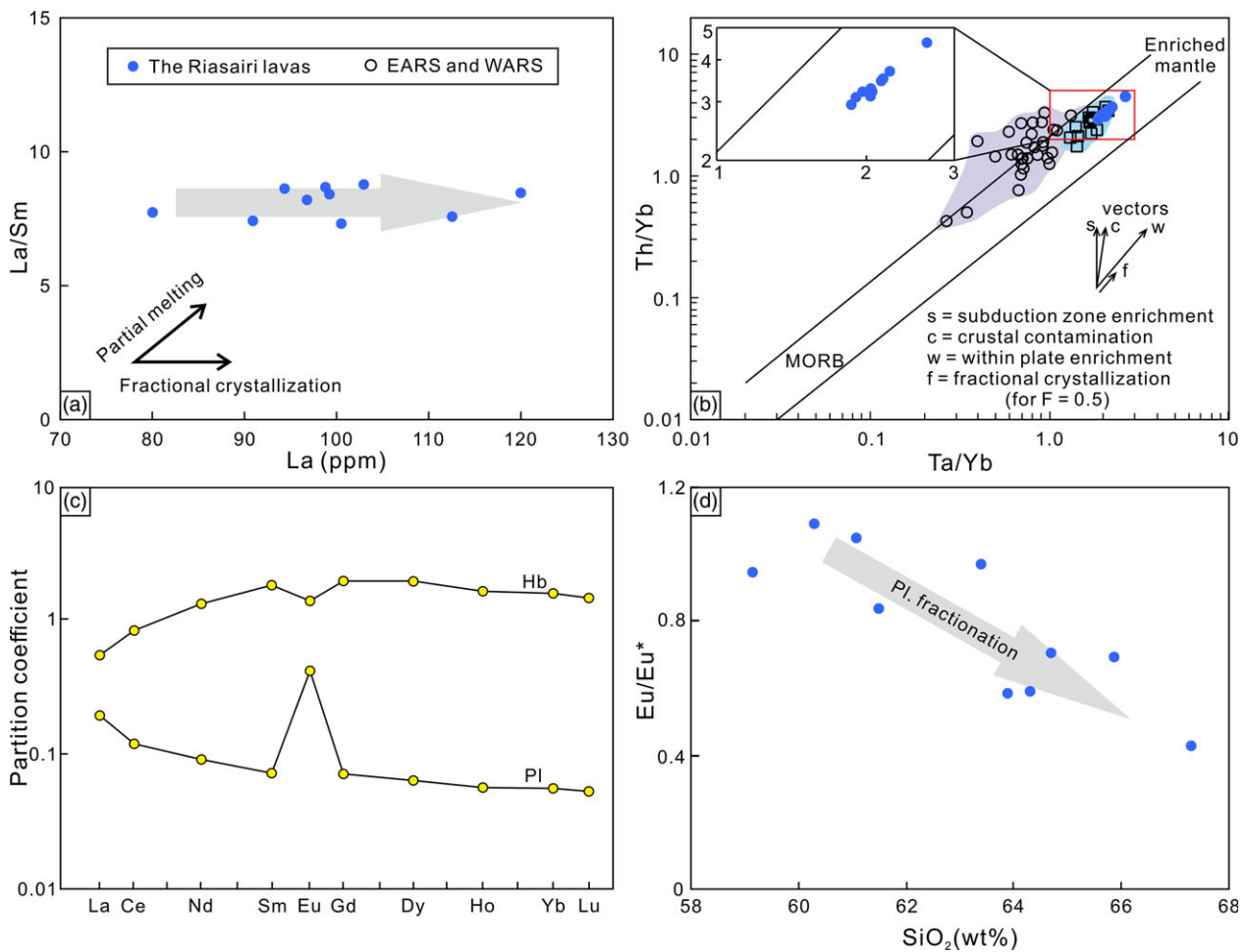
Fig. 8. (Colour online) (a) La (ppm) versus La/Sm diagram (after Allégre *et al.* 1984). (b) Ta/Yb versus Th/Yb diagram (after Pearce, 1982). (c) Plagioclase/melt and amphibole/melt partition coefficients for basalts (after Rollinson, 1993). (d) SiO₂ (wt%) versus Eu/Eu* diagram. The detailed citation data from the EARS and the WARS are given in online Supplementary Table S2 (available at http://journals.cambridge.org/geo).

We therefore propose four stages of evolution for the Riasairi lavas of the Bangong–Nuijang rift (Fig. 9). Stage 1: Upwelling asthenosphere was associated with continental rifting. During this stage the magmas mixed with partially melted continental litho-spheric mantle, acquiring the unique isotopic characteristics as dis-cussed above. Stage 2: The homogeneously mixed parent magma underwent differentiation by fractional crystallization of pyroxene and olivine to form a dominantly basaltic magma in the lower crust. Stage 3: As this magma continued to accumulate in the lower magma chamber, relatively low-density basaltic magma flooded into an overlying or adjacent shallow magma chamber in the upper crust. During this period, a large amount of hornblende and a small amount of plagioclase were precipitated from the basaltic magma, resulting in the formation of trachytic magma. Stage 4: As magma accumulated and differentiated in the magmatic chamber in the upper crust, tectonic activity or simply overpressure in the cham-ber resulted in the surface eruption of trachyandesites and trachytes.

5.d. Deposition and provenance of host sedimentary rocks

The detrital zircon population of the Mugagangri Group sandstone is marked by several modes spanning Meso-Archean to Late

Triassic time (Fig. 10d). These modes are comparable to those of the upper subunit (the Lower Mugagangri Group) described by Li *et al.* (2017), who argued that these strata were deposited in abyssal plain environments close to the Qiangtang passive mar-gin during Late Triassic time and sourced solely from the Southern Qiangtang block. It is noteworthy that the *c.* 235 Ma mode is present in Riasairi sandstone blocks (Figs 6c, 10c), although no plu-tons or volcanic rocks of that age have yet been reported in the Southern Qiangtang block (Li *et al.* 2019a). Our data suggest that this Middle–Late Triassic mode might be derived from the erosion of the Riasairi lavas and related intrusives. Rocks formed by this magmatic event are not widely exposed, which can be attributed to the strong weathering and erosion that occurred after their for-mation, or their burial in the accretionary complex during later subduction and collision events.

5.e. When was the Bangong–Nujiang Ocean born?

Despite decades of research, interpretation of the earliest geological record of the BNSZ in terms of continental rifting and incipient oceanic crust accretion remains controversial, with timing esti-mates ranging from the Carboniferous to Early Jurassic (e.g. Li *et al.* 2019b; Peng *et al.* 2020).
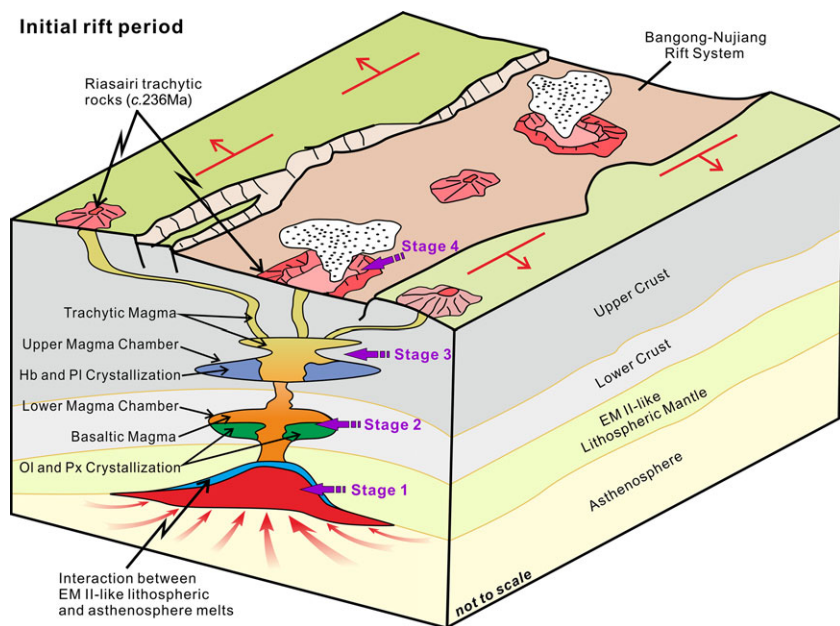
Fig. 9. (Colour online) Model of the formation of the Bangong–Nujiang rift, including four-stage evolution of the Riasairi lavas.
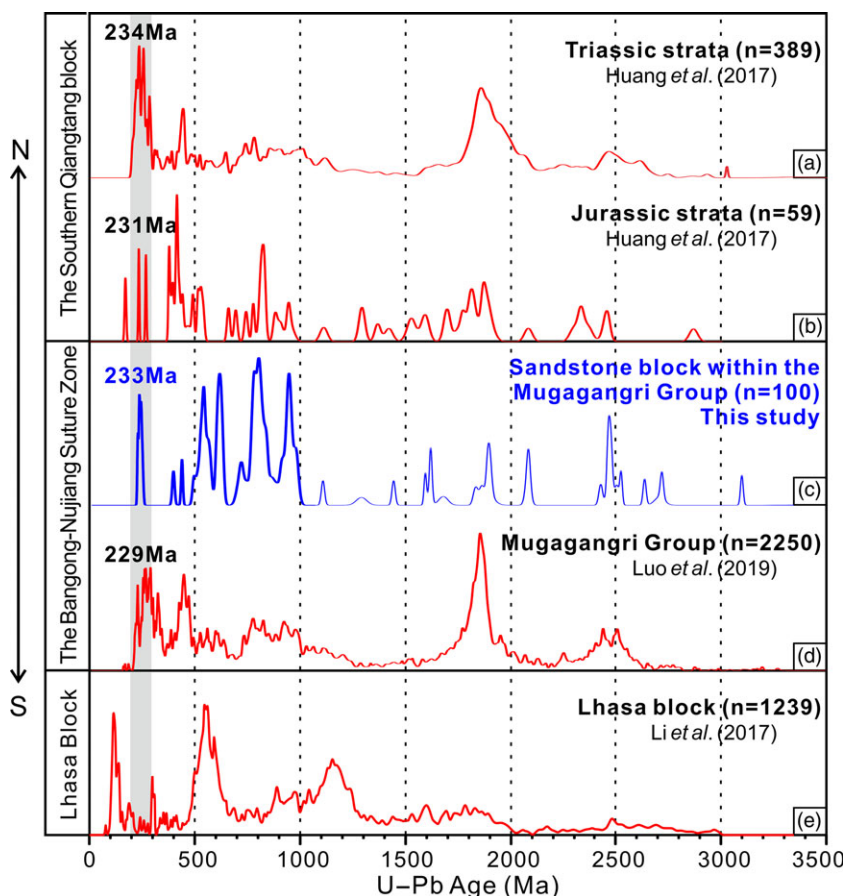

Fig. 10. (Colour online) Detrital zircon age spectra for representative strata in (a, b) the Southern Qiangtang block, (c, d) BNSZ and (e) Lhasa block. Literature age data include Huang *et al.* (2017), Li *et al.* (2017) and Luo *et al.* (2019).

5.e.1. Palaeozoic rifting?

Arguments for Permian rifting are due to the discovery of the Permian mafic dyke swarms within the Qiangtang terrane (Zhai *et al.* 2013; Xu *et al.* 2016). These magmas are interpreted to have formed during large igneous province (LIP) emplacement (Zhai *et al.* 2013) and early rifting phases (Xu *et al.* 2016). However, although LIP emplacement is often followed by continental break-up and oceanization (e.g. Dewey & Burke, 1973; van Hinsbergen *et al.* 2011), this is certainly not always the case (e.g. Siberian traps LIP), and dyke swarms may be located either near to or far from (up to 2500 km) the centre of a LIP (Ernst & Buchan, 1997), making a link to the BNO opening equivocal.
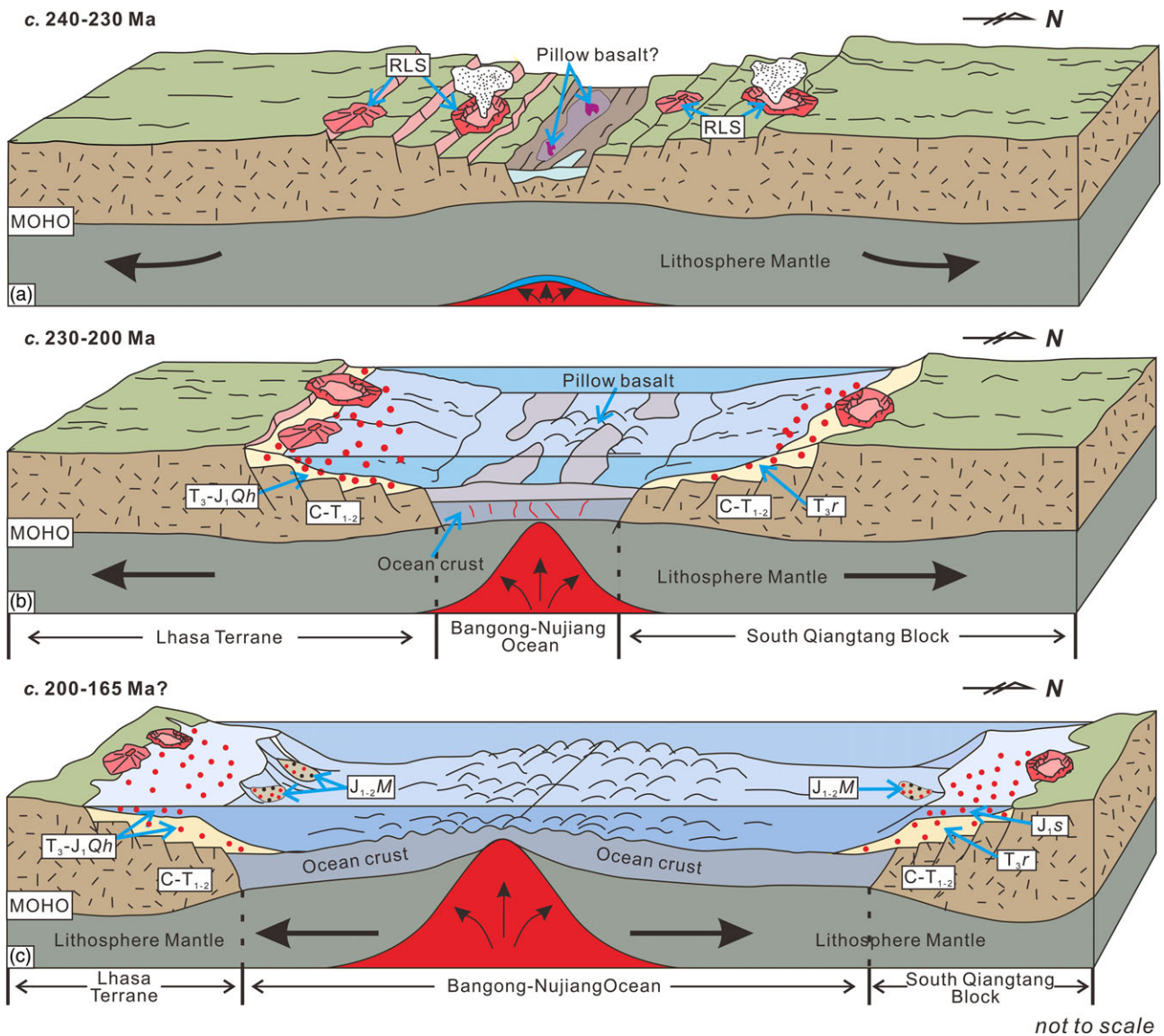
Fig. 11. (Colour online) Evolution of the Bangong–Nujiang Ocean.

Most constraints on the opening of the BNO are based on U–Pb zircon ages from BNSZ ophiolites. These ages are mostly interpreted as the age of the oceanic crust of the ophiolite, demonstrating the presence of oceanic lithosphere in the Southern Qiangtang block at that time (Qiangba *et al.* 2009; Wei *et al.* 2016; Zhang *et al.* 2016, 2017; Wu *et al.* 2018). Such ages are therefore considered as a minimum age for rifting. The oldest ophiolitic fragments in the BNSZ are latest Permian to Late Triassic in age, with massifs dated (zircon U–Pb) at *c.* 252 Ma (Wei *et al.* 2016), *c.* 222 Ma (Wu *et al.* 2018) and 217.8 ± 1.6 Ma (Qiangba *et al.* 2009). A 254 ± 28 Ma Re–Os pseudo-isochron age (Huang *et al.* 2012) from the Bangong Co ophiolite would be consistent with, but not conclusive for, a latest Permian age for the opening of BNO. Protolith ages of metamorphosed subducted oceanic crust also provide a latest Permian minimum age for opening of the BNO with zircon U–Pb dates at 260–242 Ma (Zhang *et al.* 2016, 2017). However, this 260–240 Ma oceanic crust generation is not reflected in the ophiolitic sedimentary covers. The oldest radiolarian fauna reported from abyssal sedimentary rocks of the BNSZ are of Middle Triassic age in the

Naqu area (Pan *et al.* 2006) and of Upper Triassic age in the Dengqen area (Wang *et al.* 2002*b*). Otherwise, the majority of radiolarian cherts from the BNSZ are of Jurassic age (Zhou *et al.* 1997; Wang *et al.* 2002*a, b*; Bai *et al.* 2005; Baxter *et al.* 2009), as are most ophiolites (see Li *et al.* 2019*b* for a review). This discrepancy might reflect the presence of inherited zircon in some of the ophiolites. For instance, zircon U–Pb ages for the Dong Co ophiolite alone include populations at 157.6 ± 4.3 Ma (Peng, 2016), 167 ± 2 Ma (Wang *et al.* 2016), 222 ± 4.8 Ma (Wu *et al.* 2018) and 252.1 ± 1.5 Ma (Wei *et al.* 2016). Although it is not impossible that the ophiolite was the locus of mafic magmatism for 100 Ma, the possibility of inherited zircon populations cannot be ruled out. Late Permian inherited zircon has actually been documented in the Jurassic Kangqiong ophiolite of the BNSZ (Fan *et al.* 2015). In this context, it seems hazardous to consider the zircon ophiolitic record alone to constrain the timing for the birth of the BNO. Additional constraints include the age of the Riganpeico Formation, a pre-Upper Triassic bathyal basin of the Southern Qiangtang block margin (Hou *et al.* 2018; Wang &

Fu, 2018) or the Upper Permian angular unconformity between the Upper Permian Longge Formation and the Upper Triassic Riganpeico formation (see Li *et al.* 2019*c* for a review). Indirect evidence for rifting (e.g. dyke swarms or unconformities) therefore point to a Permian rifting event, consistent with Late Permian and younger minimum age estimates from oceanic rocks. However, none of the above evidence appears unequivocal, and BNO birth estimates span over 100 Ma, leaving room for alternate hypotheses.

5.e.2. Middle Triassic rifting?

In this paper, the Riasairi trachytic lavas, formed during 238–236 Ma, provide direct geochemical evidence that they derive from intra-continental rifting. These lavas have been incorporated to the Mugagangri Group accretionary prism within the BNSZ as blocks, and must therefore have been eroded from the Southern Qiangtang continental margin. They could also have been offscraped from the BNO subducting oceanic lithosphere, but their isotopic composition is not consistent with an ocean-island origin (Figs 5b, d, 7a). However, the presence of *c.* 235 Ma detrital zircons in the contemporaneous Riasairi sandstone blocks supports the theory that they were eroded from a terrestrial source. In such a case, it is difficult to see a scenario in which these continental rift-related volcanic rocks would have formed in a setting in which the BNO already existed. These trachytes therefore show that, in the Riasairi area, the oceanization of the BNO post-dated 238–236 Ma.

This inference is consistent with Upper Triassic shallow-marine to bathyal-facies sedimentary formations that are well developed on both sides of the study area (Chen *et al.* 2002; Lu *et al.* 2002; Qu *et al.* 2003; Zheng *et al.* 2003; Yao *et al.* 2004; Zhu *et al.* 2005*a*, *b*; Wang *et al.* 2006*a*, *b*), including the Quehala Group in the Northern Lhasa block and the Riganpeicuo Group in the South Qiangtang block, which are widely distributed (Zhu *et al.* 2011). Both groups are in angular unconformable contact with the lower Permian–Lower Triassic formations (Wang & Fu, 2018), hinting at the existence of a regional tectonic event during Middle–Late Triassic time.

We propose that the BNO formed, in the Riasairi area, during the continental break-up of the southern Qiantang and northern Lhasa terranes during 240–230 Ma (Fig. 11a). From 230–200 Ma, ocean spreading of the BNO occurred allowing the N-wards flight of the Qiangtang continent(s). Shallow-marine sediments represented by the Riganpeicuo Group and the Quehala Group formed in the Southern Qiantang and Northern Lhasa blocks, respectively (Fig. 11b) (Zhu *et al.* 2011; Bo *et al.* 2017). In the BNO, the presence of Jurassic abyssal sediments of the (Lower) Mugagangri Group (Li *et al.* 2017) and evidence of volcanic activity recorded by the T_3–J_3 sedimentary rocks verify the tectonism and magmatism represented by the Riasairi rift-related lavas, which further support the opening time of the middle segment of BNO represented by the study area (Fig. 11c).

6. Conclusions

(1) The first reported Middle–Late Triassic Riasairi trachytes presented here are the earliest record of rift-related volcanic in the BNSZ so far. Their geochemical signatures are consistent with having formed in a continental rift setting and are akin to modern rift volcanic sequences (e.g. Eastern African Rift Zone and Antarctic Rift Zone).

(2) Isotopic analyses, including whole-rock Sr–Nd–Pb, demonstrate that the magma was sourced from the mixing of depleted asthenospheric mantle and partial melting of the lithospheric mantle before undergoing fractional crystallization.

(3) Based on these data, conjunction with the zircon U–Pb age obtained here (*c.* 236 Ma), we propose that the middle segment of the BNO in the Riasairi area opened during Middle–Late Triassic time.

References

Allégre CJ, Courtillot V, Tapponnier P, Hirn A, Mattauer M, Coulon C, Jaeger JJ, Achache J, Schärer U, Marcoux J, Burg JP, Girardeau J, Armijo R, Gariépy C, Göpel C, Li TD, Xiao XC, Chang CF, Li GQ, Lin BY, Teng JW, Wang NW, Chen GM, Han TL, Wang XB, Den WM, Sheng HB, Cao YG, Zhou J, Qiu HR, Bao PS, Wang SC, Wang BX, Zhou YX and Xu RH (1984) Structure and evolution of the Himalaya–Tibet orogenic belt. *Nature* **307**, 17–22. doi: 10.1038/307017a0.

Ayalew D, Barbey P, Marty B, Reisberg L, Yirgu G and Pik R (2002) Source, genesis, and timing of giant ignimbrite deposits associated with Ethiopian continental flood basalts. *Geochimica et Cosmochimica Acta* **66**, 1429–48. doi: 10.1016/s0016-7037(01)00834-1.

Ayalew D, Jung S, Romer RL, Kersten F, Pfänder JA and Garbe-Schönberg D (2016) Petrogenesis and origin of modern Ethiopian rift basalts: constraints from isotope and trace element geochemistry. *Lithos* **258–259**, 1–14. doi: 10.1016/j.lithos.2016.04.001.

Bai ZD, Xu DB, Zhang XJ, Zhu GX and Sun LX (2005) *1:250,000 geological report of Amdo with geological map*. Beijing, China: Institute of Geological Survey.

Baxter A, Aitchison J and Zyabrev S (2009) Radiolarian age constraints on Mesotethyan ocean evolution, and their implications for development of the Bangong-Nujiang suture, Tibet. *Journal of the Geological Society* **166**, 689–94. doi: 10.1144/0016-76492008-128.

Beccaluva L, Bianchini G, Natali C and Siena F (2009) Continental flood basalts and mantle plumes: a case study of the northern Ethiopian Plateau. *Journal of Petrology* **50**, 1377–403. doi: 10.1093/petrology/egp024.

Bo JF, Wang XL, Gao JH, Yao JX, Wang GH and Hou EG (2017) Upper Triassic reef coral fauna in the Renacuo area, northern Tibet, and its implications for palaeobiogeography. *Journal of Asian Earth Sciences* **146**, 114–33. doi: 10.1016/j.jseaes.2017.05.006.

Chauvet F, Lapierre H, Maury RC, Bosch D, Basile C, Cotten J, Brunet P and Campillo S (2011) Triassic alkaline magmatism of the Hawasina Nappes: post-breakup melting of the Oman lithospheric mantle modified by the Permian Neotethyan Plume. *Lithos* **122**, 122–36. doi: 10.1016/j.lithos.2010.12.006.

Chen YL, Chen GR, Zhang KZ, Zhao SR, Liu BM and Suolang GC (2002) *1:250,000 geological report of Bange County with geological map*. Beijing, China: Institute of Geological Survey.

Condie KC (1993) Chemical composition and evolution of the upper continental crust: contrasting results from surface samples and shales. *Chemical Geology* **104**, 1–37. doi: 10.1016/0009-2541(93)90140-e.

Corti G, Sani F, Agostini S, Philippon M, Sokoutis D and Willingshofer E (2018) Off-axis volcano-tectonic activity during continental rifting: insights

from the transversal Goba-Bonga lineament, Main Ethiopian Rift (East Africa). *Tectonophysics* **728**. doi: 10.1016/j.tecto.2018.02.011.

Cousens BL, Clague DA and Sharp WD (2003) Chronology, chemistry, and origin of trachytes from Hualalai Volcano, Hawaii. *Geochemistry, Geophysics, Geosystems* **4**. doi: 10.1029/2003gc000560.

Dewey J and Burke K (1973) Tibetan, Variscan, and Precambrian Basement Reactivation: products of continental collision. *Journal of Geology* **81**. doi: 10.1086/627920.

Ding QF (2017) A study on Jurassic bivalves: biostratigraphy of Duoma area in Shuanghu, Northern Tibet. M.Sc. thesis, China University of Geosciences (Beijing), Beijing, China. Published thesis.

Ernst R and Buchan KL (1997) Layered mafic intrusions: a model for their feeder systems and relationship with giant dyke swarms and mantle plume centres. *South African Journal of Geology* **100**, 319–34.

Fan JJ, Li C, Xie CM, Wang M and Chen JW (2015) The evolution of the Bangong–Nujiang Neo-Tethys ocean: evidence from zircon U–Pb and Lu–Hf isotopic analyses of Early Cretaceous oceanic islands and ophiolites. *Tectonophysics* **655**, 27–40. doi: 10.1016/j.tecto.2015.04.019.

Feyissa DH, Shinjo R, Kitagawa H, Meshesha D and Nakamura E (2017) Petrologic and geochemical characterization of rift-related magmatism at the northernmost Main Ethiopian Rift: implications for plume-lithosphere interaction and the evolution of rift mantle sources. *Lithos* **282–283**, 240–61. doi: 10.1016/j.lithos.2017.03.011.

Fontijn K, Elburg MA, Nikogosian IK, van Bergen MJ and Ernst GGJ (2013) Petrology and geochemistry of Late Holocene felsic magmas from Rungwe volcano (Tanzania), with implications for trachytic Rungwe Pumice eruption dynamics. *Lithos* **177**, 34–53. doi: 10.1016/j.lithos.2013.05.012.

Giordano F, D'Antonio M, Civetta L, Tonarini S, Orsi G, Ayalew D, Yirgu G, Dell'Erba F, Di Vito MA and Isaia R (2014) Genesis and evolution of mafic and felsic magmas at Quaternary volcanoes within the Main Ethiopian Rift: insights from Gedemsa and Fanta 'Ale complexes. *Lithos* **188**, 130–44. doi: 10.1016/j.lithos.2013.08.008.

Hart SR (1984) A large-scale isotope anomaly in the Southern Hemisphere mantle. *Nature (London)* **309**, 753–7. doi: 10.1038/309753a0.

Hastie AR, Kerr AC, Pearce JA and Mitchell (2007) Classification of altered volcanic island arc rocks using immobile trace elements: development of the Th-Co discrimination diagram. *Journal of Petrology* **12**, 2341–57. doi: 10.1093/petrology/egm062.

Hofmann AW, Jochum KP, Seufert M and White WM (1986) Nb and Pb in oceanic basalts: new constraints on mantle evolution. *Earth and Planetary Science Letters* **79**, 33–45. doi: 10.1016/0012-821x(86)90038-5.

Hoskin PWO and Black LP (2000) Metamorphic zircon formation by solid-state recrystallization of protolith igneous zircon. *Journal of Metamorphic Geology* **18**, 423–39. doi: 10.1046/j.1525-1314.2000.00266.x.

Hou EG, Chen YF, Gao JH and Wang GH (2018) U-Pb dating and its implication for the clastic sedimentary rocks in the Rigain Pünco Formation in the Niu Mountain in Nyima County, Tibet. *Earth Science Frontiers* **25**, 197–209.

Huang QS, Shi RD and Ding BH (2012) Re-Os isotopic evidence of MOR-type ophiolite from the Bangong Co for the opening of Bangong-Nujiang Tethys Ocean. *Acta Petrologica et Mineralogica* **31**, 465–78.

Huang TT, Xu JF, Chen JL, Wu JB and Zeng YC (2017) Sedimentary record of Jurassic northward subduction of the Bangong–Nujiang Ocean: insights from detrital zircons. *International Geology Review* **59**, 166–84. doi: 10.1080/00206814.2016.1218801.

Hutchison W, Mather T, Pyle D, Boyce A, Gleeson M, Yirgu G, Blundy J, Ferguson D, Vye-Brown C, Millar I, Sims K and Finch A (2018) The evolution of magma during continental rifting: new constraints from the isotopic and trace element signatures of silicic magmas from Ethiopian volcanoes. *Earth and Planetary Science Letters* **489**, 203–18. doi: 10.1016/j.epsl.2018.02.027.

Hutchison W, Pyle DM, Mather TA, Yirgu G, Biggs J, Cohen BE, Barfod DN and Lewi E (2016) The eruptive history and magmatic evolution of Aluto volcano: new insights into silicic peralkaline volcanism in the Ethiopian rift. *Journal of Volcanology and Geothermal Research* **328**, 9–33. doi: 10.1016/j.jvolgeores.2016.09.010.

Irvine TN and Baragar WRA (1971) A guide to the chemical classification of the common volcanic rocks. *Canadian Journal of Earth Sciences* **8**, 523–48. doi: 10.1139/e71-055.

Kapp P and Decelles P (2019) Mesozoic-Cenozoic geological evolution of the Himalayan-Tibetan orogen and working tectonic hypotheses. *American Journal of Science* **319**, 159–254. doi: 10.2475/03.2019.01.

Le Bas MJ, Le Maitre RW, Streckeisen A and Zanettin P (1986) A chemical classification of volcanic rocks based on the total alkalisillica diagram. *Journal of Petrology* **27**, 745–50. doi: 10.1093/petrology/27.3.745.

LeMasurier W, Choi SH, Kawachi Y, Mukasa S and Rogers N (2011) Evolution of pantellerite-trachyte-phonolite volcanoes by fractional crystallization of basanite magma in a continental rift setting, Marie Byrd Land, Antarctica. *Contributions to Mineralogy and Petrology* **162**, 1175–99. doi: 10.1007/s00410-011-0646-z.

Li C, Huang XP, Zhai QG, Zhu TX, Yu YS, Wang GH and Zeng QG (2006) The Longmu Co-Shuanghu-Jitang plate suture and the northern boundary of Gondwanaland in the Qinghai-Tibet plateau. *Earth Science Frontiers* **13**, 136–47.

Li S, Chung SL, Hou ZQ, Chew D, Wang T, Wang BD and Wang YB (2019a) Early Mesozoic magmatism within the Tibetan Plateau: implications for the Paleo-Tethyan tectonic evolution and continental amalgamation. *Tectonics* **38**, 3505–43. doi: 10.1029/2019tc005546.

Li S, Ding L, Guilmette C, Fu JJ, Xu Q, Yue Y, Hui and Henrique-Pinto R (2017) The subduction-accretion history of the Bangong-Nujiang Ocean: constraints from provenance and geochronology of the Mesozoic strata near Gaize, central Tibet. *Tectonophysics* **702**, 42–60. doi: 10.1016/j.tecto.2017.02.023.

Li S, Guilmette C, Yin CQ, Ding L, Zhang J, Wang HQ and Baral U (2019b) Timing and mechanism of Bangong-Nujiang ophiolite emplacement in the Gerze area of central Tibet. *Gondwana Research* **71**, 179–93. doi: 10.1016/j.gr.2019.01.019.

Li S, Yin CQ, Guilmette C, Ding L and Zhang J (2019c) Birth and demise of the Bangong-Nujiang Tethyan Ocean: a review from the Gerze area of central Tibet. *Earth-Science Reviews* **198**, 102907. doi: 10.1016/j.earscirev.2019.102907.

Li SM, Zhu DC, Wang Q, Zhao ZD, Zhang LL, Liu SA, Chang QS, Lu YH, Dai JG and Zheng YC (2016a) Slab-derived adakites and subslab asthenosphere-derived OIB-type rocks at 156 ± 2 Ma from the north of Gerze, central Tibet: records of the Bangong–Nujiang oceanic ridge subduction during the Late Jurassic. *Lithos* **262**, 456–69. doi: 10.1016/j.lithos.2016.07.029.

Li ZY, Ding L, Lippert P, Song PP, Yue YH and van Hinsbergen DJJ (2016b) Paleomagnetic constraints on the Mesozoic drift of the Lhasa terrane (Tibet) from Gondwana to Eurasia. *Geology* **44**, 727–30. doi: 10.1130/G38030.1.

Lu SW, Du FJ, Ren JD, Zhang YQ, Liu PD, Pei ZC, Jia GX, Xie CY and Li XZ (2002) *1:250,000 geological report of Nima Region with geological map*. Beijing, China: Institute of Geological Survey.

Ludwig KR (2003) *User's Manual for Isoplot/Ex Version 3.00, A Geochronological Toolkit for Microsoft Excel*. Berkeley: Berkeley Geochronology Center, Special Publication no. 4, 72 pp.

Luo AB, Fan JJ, Wang M and Zeng XW (2019) Age of flysch in Bangong-Nujiang Ocean: constraints of detrital zircon from Yaduo village of Gerze county. *Earth Science-Journal of China University of Geosciences* **44**, 2426.

McClellan E and Gazel E (2014) The Cryogenian intra-continental rifting of Rodinia: evidence from the Laurentian margin in eastern North America. *Lithos* **206–207**, 321–37. doi: 10.1016/j.lithos.2014.08.006.

Metcalfe I (2011) Tectonic framework and Phanerozoic evolution of Sundaland. *Gondwana Research* **19**, 3–21. doi: 10.1016/j.gr.2010.02.016.

Natali C, Beccaluva L, Bianchini G and Siena F (2011) Rhyolites associated to Ethiopian CFB: clues for initial rifting at the Afar plume axis. *Earth and Planetary Science Letters* **312**, 59–68. doi: 10.1016/j.epsl.2011.09.059.

Natali C, Beccaluva L, Bianchini G and Siena F (2013) The Axum–Adwa basalt–trachyte complex: a late magmatic activity at the periphery of the Afar plume. *Contributions to Mineralogy and Petrology* **166**, 351–70. doi: 10.1007/s00410-013-0879-0.

Pan GT, Mo XX, Hou ZQ, Zhu DC, Wang LQ, Li GM, Zhao ZD, Geng QR and Liao ZL (2006) Spatial-temporal framework of the Gangdese Orogenic Belt and its evolution. *Acta Petrologica Sinica* **22**, 521–33. doi: 10.1016/j.sedgeo.2005.12.020.

Panter KS, Kyle PR and Smellie JL (1997) Petrogenesis of a phonolite-trachyte succession at Mount Sidley, Marie Byrd Land, Antarctica. *Journal of Petrology* **38**, 1225–53. doi: 10.1093/petroj/38.9.1225.

Pearce J (1982) Trace element characteristics of lavas from destructive plate boundaries. In *Andesites: Orogenic Andesites and Related Rocks* (ed. RS Thorpe), pp. 525–48. New York: John Wiley.

Peccerillo A, Barberio MR, Yirgu G, Ayalew D, Barbieri M and Wu TW (2003) Relationships between mafic and peralkaline silicic magmatism in continental rift settings: a petrological, geochemical and isotopic study of the Gedemsa volcano, central Ethiopian rift. *Journal of Petrology* 44, 2003–32. doi: 10.1093/petrology/egg068.

Peng TP (2016) Gerze Dongcuo ophiolite plagioclase granite geochemical characteristics and zircon U-Pb chronology research in Tibet. *Geology of Fujian* 35, 259–65.

Peng YB, Yu SY, Li SZ, Liu YJ, Santosh M, Lv P, Li YS, Xie WM and Liu YM (2020) The odyssey of Tibetan Plateau accretion prior to Cenozoic India-Asia collision: probing the Mesozoic tectonic evolution of the Bangong-Nujiang Suture. *Earth-Science Reviews* 211. doi: 10.1016/j.earscirev.2020.103376.

Qiangba Z, Xie YW, Wu YW, Xie CM, Li QL and Qiu JQ (2009) Zircon SIMS U-Pb dating and its significance of cumulate gabbro from Dengqen ophiolite, eastern Tibet. *Geological Bulletin of China* 28, 1253–8.

Qiu RZ, Zhou S, Deng JF, Li JF, Xiao QH and Cai ZY (2004) Dating of gabbro in the Shemalagou ophiolite in the western segment of the Bangong Co-Nujiang ophiolite belt, Tibet – with a discussion of the age of the Bangong Co-Nujiang ophiolite belt. *Geology in China* 31, 262–8.

Qu YG, Wang YS, Duan JX, Zhang SQ, Wang ZH, Lv P, Liu GZ, Li XB, Feng DC, Xie YH, Yu XW, Jiang XF, Sun ZG, Li QW, Liang SF, Wang HS and Guo SS (2003) *1:250,000 geological report of Duoba Region with geological map*. Beijing, China: Institute of Geological Survey.

Ren JS and Xiao LW (2004) Lifting the mysterious veil of the tectonics of the Qinghai-Tibet Plateau by 1:250,000 geological mapping. *Geological Bulletin of China* 23, 1–11.

Rollinson H (1993) *Using Geochemical Data: Evaluation, Presentation, Interpretation*. London: Longman Scientific and Technical.

Shu QH, Lai Y, Zhou YT, Xu JJ and Wu HY (2015) Zircon U–Pb geochronology and Sr–Nd–Pb–Hf isotopic constraints on the timing and origin of Mesozoic granitoids hosting the Mo deposits in northern Xilamulun district, NE China. *Lithos* 238, 64–75. doi: 10.1016/j.lithos.2015.09.014.

Sun SS and McDonough WF (1989) Chemical and isotopic systematics of oceanic basalts: implications for mantle composition and processes. In *Magmatism in the Ocean Basins* (eds AD Saunders and MJ Norry), pp. 313–45. Geological Society of London, Special Publication no. 42,. doi: 10.1144/GSL.SP.1989.042.01.19.

Tang Y, Zhai QG, Chung Sun-Lin, Hu PY, Wang J, Xiao XC, Song B, Wang HT and Lee HY (2020) First mid-ocean ridge-type ophiolite from the Meso-Tethys suture zone in the north-central Tibetan plateau. *GSA Bulletin* 132, 2202–20. doi: 10.1130/B35500.1.

Taylor SR and McLennan SM (1985) *The Continental Crust: Its Composition and Evolution*. Oxford: Blackwell Scientific Publication.

Trua T, Deniel C and Mazzuoli R (1999) Crustal control in the genesis of Plio-Quaternary bimodal magmatism of the Main Ethiopian Rift (MER): geochemical and isotopic (Sr, Nd, Pb) evidence. *Chemical Geology* 155, 201–31. doi: 10.1016/S0009-2541(98)00174-0.

Turner S, Caulfield J, Rushmer T, Turner M, Cronin S, Smith I and Handley H (2012) Magma evolution in the primitive, intra-oceanic Tonga Arc: rapid petrogenesis of dacites at Fonualei Volcano. *Journal of Petrology* 53, 1231–53. doi: 10.1093/petrology/egs005.

van Hinsbergen DJJ, Kapp P, Dupont-Nivet G, Lippert PC, DeCelles PG and Torsvik TH (2011) Restoration of Cenozoic deformation in Asia and the size of Greater India. *Tectonics* 30. doi: 10.1029/2011TC002908.

Vervoort JD and Kemp AIS (2016) Clarifying the zircon Hf isotope record of crust–mantle evolution. *Chemical Geology* 425, 65–75. doi: 10.1016/j.chemgeo.2016.01.023.

Wang BD, Wang LQ, Chung S-L, Chen JL, Yin FG, Liu H, Li XB and Chen LK (2016) Evolution of the Bangong–Nujiang Tethyan ocean: insights from the geochronology and geochemistry of mafic rocks within ophiolites. *Lithos* 245, 18–33. doi: 10.1016/j.lithos.2015.07.016.

Wang BD, Wang LQ, Xu JF, Chen L, Zhao WX, Liu H, Peng TP and Li XB (2015) The discovery of high-pressure granulite at Shelama in Dongco area along the Bangong Co-Nujiang River suture zone and its tectonic significance. *Geological Bulletin of China* 34, 1605–16.

Wang J and Fu XG (2018) Sedimentary evolution of the Qiangtang Basin. *Geology in China* 45, 237–59.

Wang JP, Liu YM, Li QS, Yue GL and Pei F (2002a) Stratigraphic division and geological significance of the Jurassic cover sediments in the eastern sector of the Bangong Lake-Dgngqgn ophiolite belt in Tibet. *Geological Bulletin of China* 21, 405–10.

Wang M, Peng SY, Li C and Zhang TY (2019) Palaeontology and U–Pb detrital zircon geochronology of Upper Triassic strata on the northern margin of the Bangong Co–Nujiang suture zone, Tibet: constraints on the age of opening of the Meso-Tethys. *Journal of Asian Earth Sciences* 175, 26–34. doi: 10.1016/j.jseaes.2018.08.015.

Wang YJ, Wang JP and Pei F (2002b) A late Triassic radiolarian fauna in the Dingqing Ophiolite Belt, Xizang (Tibet). *Acta Micropalaeontologica Sinica* 19, 323–36.

Wang YS, Zhang SQ, Xie YH, Li CZ, Yu XW, Zheng CZ, Feng DC, Wang ZH, Duan JX, Sun ZG, Li QW, Lu ZL, Jiang XF, Lv P, Li XB, Liu GZ and Wang HS (2006a) *1:250,000 geological report of Ang'daercuo with geological map*. Beijing, China: Institute of Geological Survey.

Wang YS, Zhang SQ, Xie YH, Li CZ, Yu XW, Zheng CZ, Feng DC, Wang ZH, Duan JX, Sun ZG, Li QW, Lu ZL, Jiang XF, Lv P, Li XB, Liu GZ and Wang HS (2006b) *1:250,000 geological report of Paducuo with geological map*. Beijing, China: Institute of Geological Survey.

Weaver BL (1991) The origin of ocean island basalt end-member compositions: trace element and isotopic constraints. *Earth and Planetary Science Letters* 104, 381–97. doi: 10.1016/0012-821X(91)90217-6.

Wei SG, Song Y and Tang JX (2016) Geochemistry and geochronology of intra-oceanic subduction of the Bangong-Nujiang Tethyan Ocean during Late Permian (ca. 252 Ma). *Geological Review* 62, 194–6.

Wu Y, Chen SY, Qin MK, Guo DF, Guo GL, Zhang C and Yang JS (2018) Zircon U-Pb ages of Dongcuo Ophiolite in western Bangonghu-Nujiang suture zone and their geological significance. *Earth Science* 43, 1070–84.

Xu W, Dong YS, Zhang XZ, Deng MR and Zhang L (2016) Petrogenesis of high-Ti mafic dykes from Southern Qiangtang, Tibet: implications for a ca. 290 Ma large igneous province related to the early Permian rifting of Gondwana. *Gondwana Research* 36, 410–22. doi: 10.1016/j.gr.2015.07.016.

Yao HZ, Duan QF, Niu ZJ, Bai YS, Wang JX, Gan JM, Wei JQ, Duan WJ, Pu JJ, Zhu YH, Zeng BF, Sheng XC, Xu AW, Zhang RJ, Yuan ZX and Jv XY (2004) *1:250,000 geological report of Chibuzhangcuo with geological map*. Beijing, China: Institute of Geological Survey.

Yin A and Harrison TM (2000) Geologic evolution of the Himalayan-Tibetan Orogen. *Annual Review of Earth and Planetary Sciences* 28, 211–80. doi: 10.1146/annurev.earth.28.1.211.

Zeng M, Zhang X, Cao H, Ettensohn FR, Cheng WB and Lang XH (2016) Late Triassic initial subduction of the Bangong-Nujiang Ocean beneath Qiangtang revealed: stratigraphic and geochronological evidence from Gaize, Tibet. *Basin Research* 28, 147–57. doi: 10.1111/bre.12105.

Zhai QG, Jahn B-M, Su L, Ernst RE, Wang KL, Zhang RY, Wang J and Tang SH (2013) SHRIMP zircon U–Pb geochronology, geochemistry and Sr–Nd–Hf isotopic compositions of a mafic dyke swarm in the Qiangtang terrane, northern Tibet and geodynamic implications. *Lithos* 174, 28–43. doi: 10.1016/j.lithos.2012.10.018.

Zhang XZ, Wang Q, Dong YS, Zhang CF, Li QY, Xia XP and Xu W (2017) High-pressure granulite facies overprinting during the exhumation of eclogites in the Bangong-Nujiang Suture Zone, Central Tibet: link to flat-slab subduction. *Tectonics* 36, 2918–35. doi: 10.1002/2017TC004774.

Zhang YX, Li ZW, Zhu LD, Zhang KJ, Yang WG and Jin X (2016) Newly discovered eclogites from the Bangong Meso-Tethyan suture zone (Gaize, central Tibet, western China): mineralogy, geochemistry, geochronology, and tectonic implications. *International Geology Review* 58, 574–87. doi: 10.1080/00206814.2015.1096215.

Zheng YY, He JS, Li WJ, Zou QG, Zhao PJ, Ci Q, Zeren Z and Xu RK (2003) *1:250,000 geological report of Zigetangcuo with geological map*. Beijing, China: Institute of Geological Survey.

Zhou MF, Malpas J, Robinson PT and Reynolds PH (1997) The dynamothermal aureole of the Donqiao ophiolite (northern Tibet). *Canadian Journal of Earth Sciences* 34, 59–65. doi: 10.1139/e17-005.

Zhu DC, Zhao ZD, Niu YL, Mo XX, Chung SL, Hou ZQ, Wang LQ and Wu FY (2011) The Lhasa Terrane: record of a microcontinent and its histories of drift and growth. *Earth and Planetary Science Letters* **301**, 241–55. doi: 10. 1016/j.epsl.2010.11.005.

Zhu TX, Dong H, Shi WL, Li HR and Ou CS (2005a) *1:250,000 geological report of Tucuo with geological map.* Beijing, China: Institute of Geological Survey.

Zhu TX, Li ZL, Zhang HH, Zhang QY, Zhang ZG, Fan YN and Zhou MK (2005b) *1:250,000 geological report of Jiang'aidarina with geological map.* Beijing, China: Institute of Geological Survey.

Zindler A and Hart S (1986) Chemical geodynamics. *Annual Review of Earth and Planetary Sciences* **14**, 493–571. doi: 10.1146/annurev.ea.14.050186. 002425.